# Bow Shocks, Wiggling Jets, and Wide#Angle Winds: A High#Resolution Study of the Entrainment Mechanism of the PV Cephei Molecular (CO) Outflow

## Citation

Arce, Hector G., and Alyssa A. Goodman. 2002. "Bow Shocks, Wiggling Jets, and Wide#Angle Winds: A High#Resolution Study of the Entrainment Mechanism of the PV Cephei Molecular (CO) Outflow." The Astrophysical Journal 575 (2): 928–49. https://doi.org/10.1086/341426.

## Permanent link

http://nrs.harvard.edu/urn-3:HUL.InstRepos:41397479

## Terms of Use

# Share Your Story

Accessibility

# BOW SHOCKS, WIGGLING JETS, AND WIDE-ANGLE WINDS: A HIGH-RESOLUTION STUDY OF THE ENTRAINMENT MECHANISM OF THE PV CEPHEI MOLECULAR (CO) OUTFLOW

HÉCTOR G. ARCE[1] AND ALYSSA A. GOODMAN
Harvard-Smithsonian Center for Astrophysics, 60 Garden Street, Cambridge, MA 02138; harce@cfa.harvard.edu, agoodman@cfa.harvard.edu

## ABSTRACT

We present a new set of high-resolution molecular-line maps of the gas immediately surrounding various Herbig-Haro (HH) knots of the giant HH flow HH 315 from the young star PV Cephei. The observations, aimed at studying the entrainment mechanism of the 2.6 pc–long HH 315 flow, include IRAM 30 m maps of the $^{12}$CO (2–1), $^{12}$CO (1–0), and $^{13}$CO (1–0) lines, with beam sizes of 11″, 21″, and 22″, respectively. We compare the morphology and the kinematics of the outflow gas, as well as the temperature and momentum distribution of the molecular outflow, with those predicted by different entrainment models. With our detailed study we are able to conclude that jet bow shock entrainment by an episodic stellar wind, with a time-varying axis, produces most of the high-velocity molecular outflow observed far from the source. In addition, near PV Cep we find evidence for a poorly collimated, wide-angle molecular outflow *and* a collimated, wiggling jet–like molecular outflow. We propose that the poorly collimated component is entrained by a wide-angle wind and the collimated component is entrained by a variable jet with internal working surfaces. If this picture is true, then a stellar wind model that allows for the coexistence of a wide-angle component *and* a collimated (jetlike) stellar wind component is needed to explain the observed properties of the PV Cep outflow. The wiggling axis of the redshifted molecular outflow lobe indicates that the outflow ejection axis is changing over time. We find that the timescale of the axis variation shown by the molecular outflow lobe is about a factor of 10 less than that shown by the large-scale optical HH knots.

*Subject headings:* ISM: Herbig-Haro objects — ISM: individual (HH 315, PV Cephei) — ISM: jets and outflows — stars: formation

## 1. INTRODUCTION

In order to better understand the effects of winds from young stars on the ambient molecular cloud, it is essential to study how the wind interacts with its surrounding medium. The best evidence that winds from young stars interact with their surrounding ambient gas is the existence of molecular outflows. Many molecular outflows have masses that are larger than their powering young star, by a factor of a few up to an order of magnitude (e.g., Wu, Huang, & He 1996). It is, therefore, highly unlikely that the mass in CO outflows comes directly from the forming star and/or the circumstellar disk, and so molecular outflows consist mainly of swept-up ambient material.

The mechanism by which a wind from a young stellar object entrains and accelerates the ambient gas, thereby producing a molecular outflow, is still a matter of debate, even though several models have been proposed. The three most popular entrainment models are the turbulent jet model, the bow shock model, and the wide-angle–wind model.

In the turbulent jet entrainment model (e.g., Cantó & Raga 1991; Stahler 1994; Lizano & Giovanardi 1995), the ambient gas is entrained on the sides of a jet (or wind) through a turbulent viscous mixing layer formed by Kelvin-Helmholtz instabilities.

In the bow shock model (e.g., Raga & Cabrit 1993; Stone & Norman 1993a; Masson & Chernin 1993; Stone & Norman 1994; Suttner et al. 1997; Zhang & Zheng 1997; Smith,

Suttner, & Yorke 1997; Downes & Ray 1999; Lee et al. 2001), a highly supersonic collimated wind or jet propagates into the ambient medium, forming a bow shock surface at the head of the jet. The jet carves into the cloud, and the bow shock moves away from the star, interacting with the ambient gas, thereby producing a molecular outflow around the jet. Velocity variations in the jet produce bow shocks along the body of the jet, also referred to as internal working surfaces (e.g., Raga et al. 1990; Raga & Kofman 1992; Cantó, Raga, & D'Alessio 2000), which can also help entrain ambient gas.

In the wide-angle–wind model (Shu et al. 1991; Li & Shu 1996; Matzner & McKee 1999; Lee et al. 2000, 2001), the outflow is produced when a momentum-conserving wide-angle wind from a young stellar object interacts with the ambient gas. The wind power is dependent on polar angle, has a constant velocity, and blows into a core with radial density profile and angular dependence. The ambient medium is swept up into a shell by a shock at the wind bubble–ambient cloud interface. The molecular outflow is then identified as the molecular gas in the entrained shell.

In Figure 1 we summarize the expected molecular outflow characteristics (i.e., gas morphology and temperature, velocity, and momentum distributions) for these three entrainment models.

On the observational front, recent high angular resolution studies of molecular outflows (e.g., Richer, Hills, & Padman 1992; Bence, Richer, & Padman 1996; Cernicharo & Reipurth 1996; Lada & Fich 1996; Davis, Smith, & Moriarty-Schieven 1998; Shepherd et al. 2000; Gueth & Guilloteau 1999; Yu, Billawala, & Bally 1999, hereafter YBB; Davis et al. 2000; Lee et al. 2000; Arce & Goodman 2001b)

---

[1] Now at Astronomy Department, California Institute of Technology, MS 105-24, Pasadena, CA 91125; harce@astro.caltech.edu.
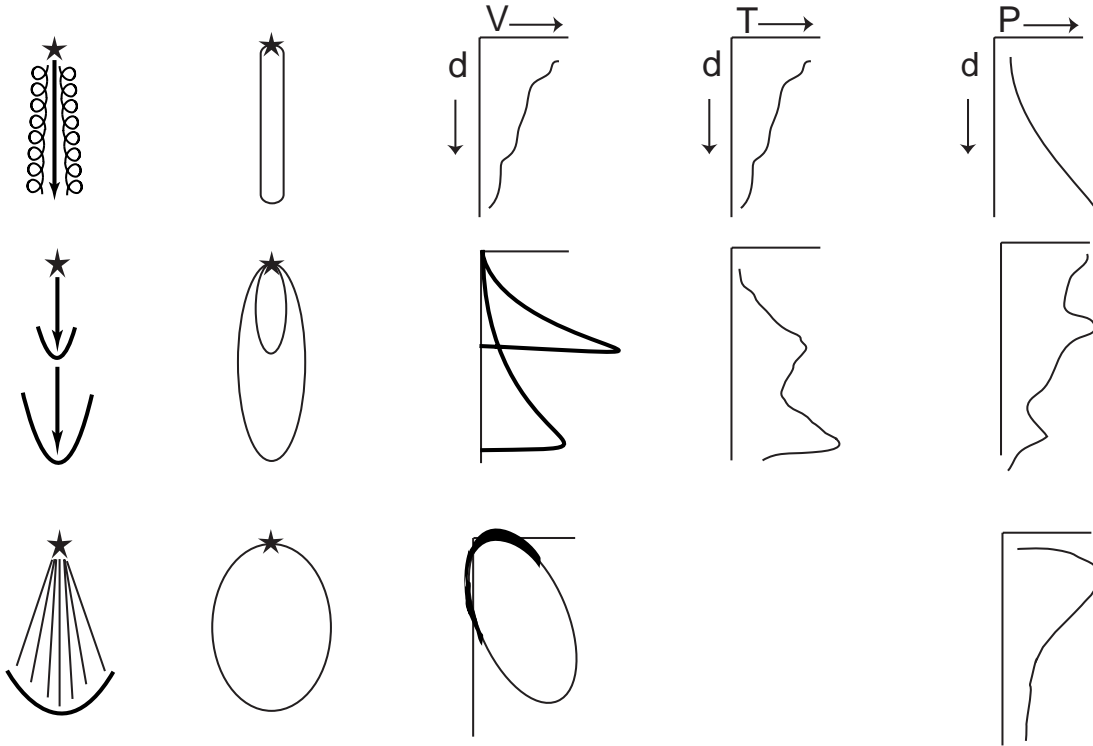
FIG. 1.—Molecular outflow properties predicted by different entrainment models. The rows, starting on the top, show the turbulent jet, jet bow shock, and wide-angle–wind properties. The columns, starting from the left, show a schematic picture of the stellar wind and the model-predicted molecular outflow morphology, velocity profile, temperature profile, and momentum profile. An underlying density distribution of $r^{-1}$ to $r^{-2}$ is assumed for the momentum profiles shown. There are no explicit estimates of the outflow gas temperature, as a function of distance from the source, for the wide-angle wind driven models. References for the turbulent jet model properties shown here are Bence et al. (1996), Cantó & Raga (1991), and Chernin & Masson (1995). References for the jet bow shock model properties shown here are Lee et al. (2001), Hatchell et al. (1999), Chernin & Masson (1995), and Cliffe, Frank, & Jones (1996). References for the wide-angle model properties shown here are Lee et al. (2001) and Li & Shu (1996).

have provided important information on the physical parameters of outflows and the entrainment mechanism.

In Arce & Goodman (2002, hereafter Paper I) we studied the interaction of the HH 315 flow with its parent cloud on large scales (see Paper I for a brief description of HH 315). In this paper, we zoom in on the gas immediately surrounding several HH knots and the outflow source (PV Cep), in order to study the entrainment mechanism of the HH 315 outflow. In particular, we study the temperature distribution, kinematics, momentum distribution, and morphology of the outflow gas. The results are then used to compare all of these observed outflow characteristics with those expected from different entrainment models. Along with the information from earlier high-resolution studies, our results provide important constraints to be considered by future theoretical entrainment models.

In the following section we will describe the observations. This is followed by a section where we describe our results. We later use our results to compare them with the results of the three molecular outflow entrainment models shown in Figure 1. Subsequently, we discuss the episodic and wandering (or wiggling) nature of the HH 315 outflow. Last, we give a summary of our findings.

## 2. OBSERVATIONS

In order to study in detail the interaction between the HH 315 flow and the surrounding gas, we made high spatial and velocity resolution observations of the gas around several of the HH knots in the flow. The data were obtained using the

IRAM 30 m telescope in Pico Veleta, Spain, in 1999 September. The $^{12}CO$ (1–0), $^{12}CO$ (2–1), and $^{13}CO$ (1–0) lines were observed simultaneously using three spectral-line SIS receivers. The spectrometer used was an autocorrelator split into three parts, each connected to a different receiver. The $J = 1 \rightarrow 0$ lines were observed with a spectral resolution of 40 kHz and a band width of 20 MHz, and the $^{12}CO$ (2–1) line was observed with a spectral resolution of 80 kHz and a band width of 40 MHz. The telescope beamwidths (FWHM) at $^{12}CO$ (1–0), $^{12}CO$ (2–1), and $^{13}CO$ (1–0) are about 21″, 11″, and 22″, respectively. The forward efficiency ($F_{eff}$) and main-beam efficiency ($B_{eff}$) of the $J = 1 \rightarrow 0$ lines are approximately 0.90 and 0.54, respectively, and for the $^{12}CO$ (2–1) line $F_{eff} \sim 0.86$ and $B_{eff} \sim 0.42$ (Wild 1999). Unless it is stated otherwise, the intensity scale of the spectral data from the IRAM 30 m is in units of main-beam temperature ($T_{mb}$), where $T_{mb} = (F_{eff}/B_{eff})T_A^*$ (Wild 1999; Rohlfs & Wilson 2000).

The on-the-fly (OTF) mapping technique was used to map three regions of interests. The telescope in OTF mode moved across the source at a constant speed of 2″ s$^{-1}$, while a spectrum was acquired every 2 s. Table 1 lists the center position and the size of each of the three major regions (see also Fig. 2). The regions were all scanned in both the right ascension and declination directions. The separation, in the direction perpendicular to the scanning direction, between subsequent rows was 4″.

The telescope was pointed to an OFF position, located at R.A. 20$^h$45$^m$30$^s$.4, decl. 67°55′46″.7 (B1950.0), after every other row, where it would observe the OFF position for

## TABLE 1
### REGIONS MAPPED WITH THE IRAM 30 METER TELESCOPE

| | CENTER POSITION | | REGION SIZE |
| REGION NAME | $\alpha_{B1950.0}$ | $\delta_{B1950.0}$ | (arcmin) |
|---|---|---|---|
| hh315b+c ........ | 20 44 49.4 | 67 52 49 | $5.2 \times 4.2$ |
| hh215 .............. | 20 45 26.4 | 67 46 13 | $2.2 \times 4.2$ |
| hh315e ............. | 20 45 59.6 | 67 40 31 | $2.3 \times 2.3$ |

NOTE.—Units of right ascension are hours, minutes, and seconds, and units of declination are degrees, arcminutes, and arcseconds.

10–15 s. A temperature calibration was done every 5–10 minutes. Deep observations of the OFF position showed no significant emission. The different regions were observed several times to improve the signal-to-noise ratio (S/N) in the spectra. The raw OTF data were reduced using CLASS. A baseline was fitted to and subtracted from each spectrum. The spectral maps of each region were convolved with Gaussian beams of different sizes, and Table 2 shows the resultant rms noise for each spectral-line map convolved with different beams.

## 3. RESULTS

### 3.1. *The Region Surrounding HH 315B and HH 315C*

Large-scale CO maps of the outflow associated with PV Cep (Levreault 1984; Paper I) show that the region surrounding the optical knots HH 315B and HH 315C (region hh315b+c) is the area where most of the emission from the northern (mostly blueshifted) outflow lobe resides (see Fig. 2). In this section, we present high spatial resolution maps of hh315b+c, which show the structure of the outflowing gas in detail and its spatial relation with the HH knots.

#### 3.1.1. $^{12}$CO (2–1) *Emission*

Figure 3 shows $^{12}$CO (2–1) velocity-integrated maps of the hh315b+c region, observed with the IRAM 30 m telescope, for 10 different velocity ranges. The emission with the
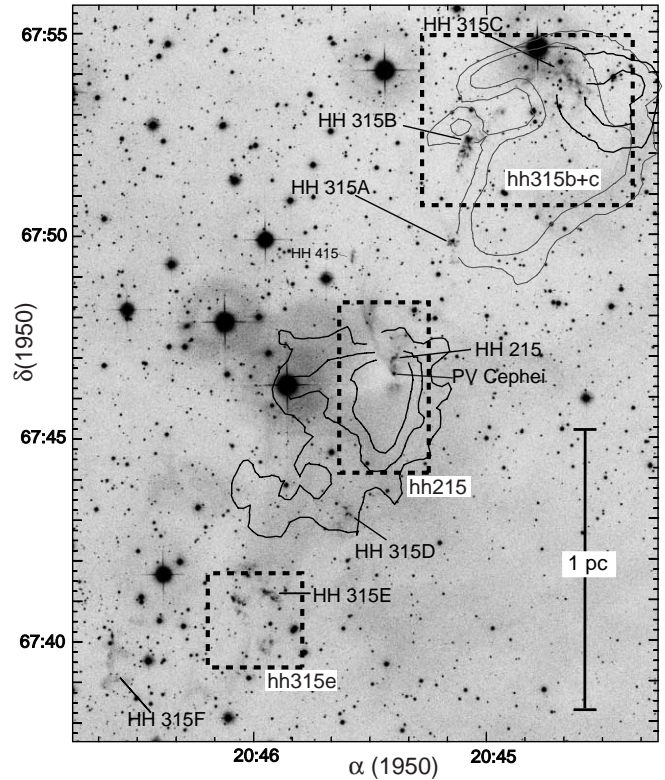


FIG. 2.—Wide-field H$\alpha$+[S II] (optical) CCD image of the HH 315 giant HH flow, from RBD. The dashed boxes denote the areas mapped with OTF mapping at the IRAM 30 m telescope. The name given to each region is shown at the bottom of each region. We also show selected contours of the large-scale blueshifted (*gray*) and redshifted (*black*) $^{12}$CO (2–1) outflow gas (based on Fig. 1 of Paper I). In certain places the contours are cut so that features in the optical image may be seen better. The position of the HH knots and the position of PV Cep (the outflow source) are also shown.

most blueshifted velocities is shown in Figure 3*b*, and the emission with the most redshifted velocities is shown in Figure 3*l*. Notice that not all velocity integration ranges have the same width. The different ranges of integration were chosen to group different channels with similar $^{12}$CO (2–1)

## TABLE 2
### rms NOISE AND VELOCITY RESOLUTION OF SPECTRAL-LINE MAPS

| Region Name | Molecular Line | Beam[a] (arcsec) | $\delta v$[b] (km s$^{-1}$) | rms[c] (K) | Where Used |
|---|---|---|---|---|---|
| hh315b+c ........ | $^{12}$CO (2–1) | 21 | 0.22 | 0.62 | Fig. 3 |
| | $^{13}$CO (1–0) | 21 | 0.22 | 0.20 | Fig. 5 |
| | $^{12}$CO (2–1) | 24 | 0.22 | 0.50 | Figs. 11 and 13 |
| | $^{12}$CO (1–0) | 24 | 0.22 | 0.28 | Figs. 11 and 14; mass estimates[d] |
| | $^{13}$CO (1–0) | 24 | 0.22 | 0.16 | Mass estimates[d] |
| hh215 .............. | $^{12}$CO (2–1) | 14 | 0.11 | 0.78 | Fig. 6 |
| | $^{13}$CO (1–0) | 14 | 0.11 | 0.28 | Fig. 7 |
| | $^{12}$CO (2–1) | 24 | 0.11 | 0.49 | Fig. 12 |
| | $^{12}$CO (1–0) | 24 | 0.11 | 0.31 | Figs. 12 and 16; mass estimates[e] |
| | $^{13}$CO (1–0) | 24 | 0.11 | 0.18 | Mass estimates[e] |
| hh315e ............. | $^{12}$CO (2–1) | 21 | 0.11 | 0.69 | Fig. 10 |

[a] Size of OTF map convolution beam. The size of each pixel in each map is always half the size of the convolution beam.
[b] Velocity resolution (width of velocity channel).
[c] Maximum rms (in $T_{mb}$ units) of all pixels *not* at the edge of the map.
[d] Outflow mass estimates of the hh315b+c region are shown in Table 3.
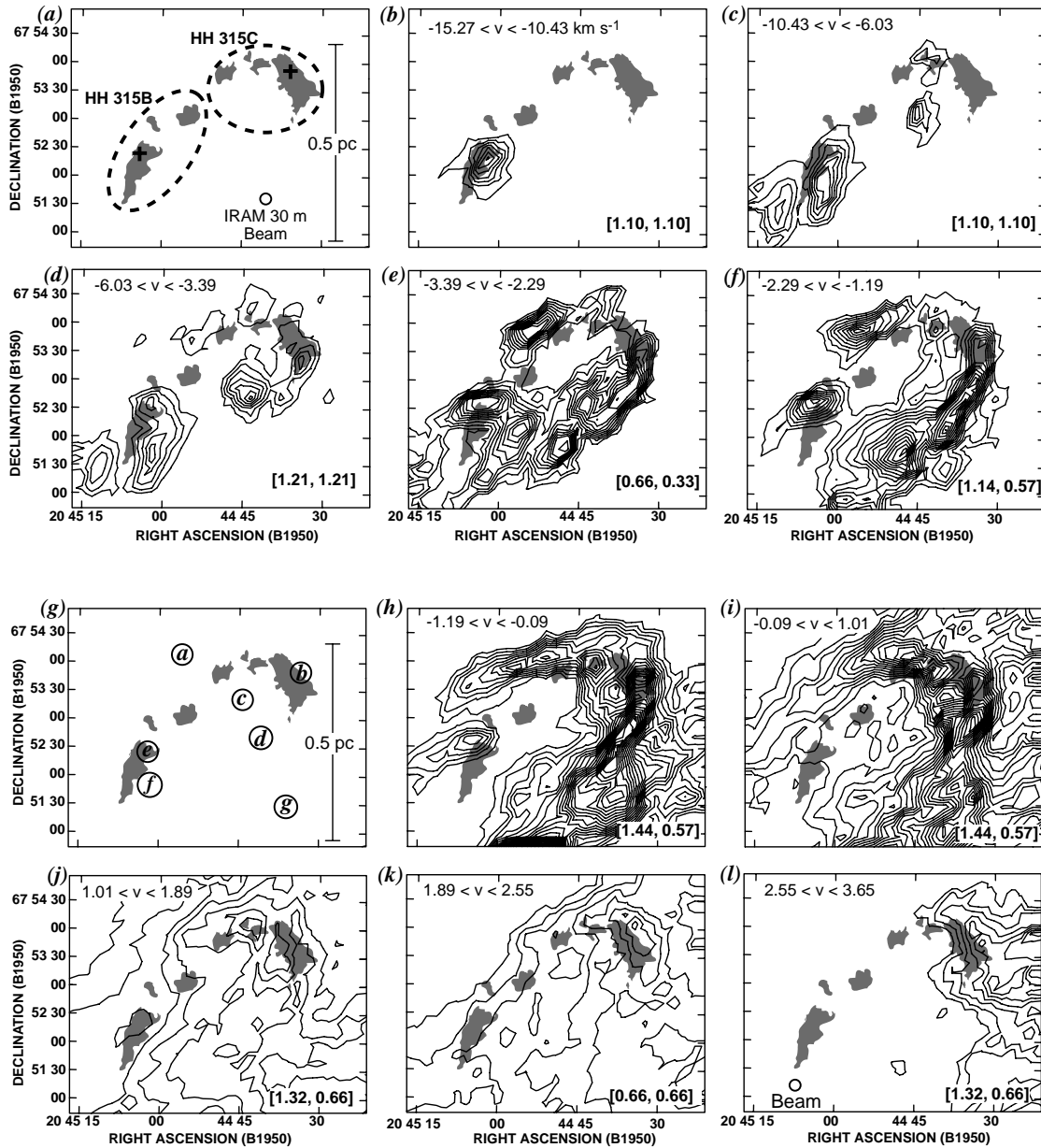[e] Outflow mass estimates of hh215 region are shown in Table 4.

FIG. 3.—Velocity-range–integrated intensity maps of the $^{12}$CO (2–1) emission surrounding the blueshifted optical knots HH 315C and HH 315B (i.e., the hh315b+c region; see Fig. 2). The velocity range of integration is shown in the upper left corner of each panel. The starting contour and the contour steps are given in brackets at the lower right corner of each panel in units of K km s$^{-1}$. The gray silhouettes represent the S [II] knots in the region, from GKW. The optical knots are identified in panel $a$. Panel $a$ also shows the IRAM 30 m beam at the $^{12}$CO (2–1) frequency (11″) and the linear scale assuming a distance to PV Cep of 500 pc. In panel $g$ we show the position from where the spectra, shown in Fig. 4, are taken. Each letter in panel $g$ represents the position of the spectrum shown in the panel (in Fig. 4) with the same letter.

emission structure. The gray objects shown in each velocity map panel represent the position of the different S [II] knots in the region, as presented by Gómez, Kenyon, & Whitney (1997, hereafter GKW).

The highest velocity (most blueshifted) CO outflow emission is shown in Figure 3$b$. The gas at these velocities is concentrated at the position of the HH 315B optical knot. The lowest (plotted) contour of integrated emission shows wing-like extensions that point toward the position of the outflow source (PV Cep). The shape of the contours at these high velocities is suggestive of a bow shock morphology.

At slightly lower (less blueshifted) velocities, the outflow gas is concentrated along the main HH 315B optical knot (see Figs. 3$c$ and 3$d$). The gas emission surrounding HH 315B in Figures 3$c$ and 3$d$ is mainly concentrated south of the emission peak in Figure 3$b$ and has an elongated morphology toward the position of PV Cep. This is consistent with a picture where the highest velocities are at the head of the shock (Fig. 3$b$), where the gas is currently being entrained, and the slower wake of previously entrained gas is found behind the head of the shock (emission in Figs. 3$c$ and 3$d$ near HH 315B).

The most striking feature of the velocity maps shown in Figure 3 is the bow shock–like (or shell-like) structure of the $^{12}$CO (2–1) emission, coincident with the bow shock–like HH 315C optical knot. The head of the CO shell coincides with the region of brightest optical emission from HH 315C and has wings, on both sides of the head, that point in the

general direction of PV Cep. Hereafter we will refer to this structure as the HH 315C CO shell. The HH 315C CO shell is observed at different outflow velocities (see Fig. 3), and at the slowest (less blueshifted) outflow velocities it has a width of about 0.4 pc (see Figs. 3h and 3i). The positional coincidence of HH 315C and the outflowing CO shell, in addition to the bow shock structure of both the optical knot and the CO outflow, is highly suggestive that these are two different outflow manifestations from the same ejection episode.

It is interesting to note that even though HH 315C is expected[2] to have a velocity of $\sim$100 km s$^{-1}$, the outflowing gas associated with the HH 315C CO shell has radial outflow velocities of no more than $\sim$5 km s$^{-1}$ (which at most could indicate maximum true space outflow velocities of about 30 km s$^{-1}$, if we assume that the angle between the flow axis and the plane of the sky is about 10°). The disparity between the velocity of optical HH knots and the velocity of their corresponding CO outflow has always been a puzzle. In a momentum-conserving interaction one would expect the more massive component to end up with a slower velocity than the less massive component. So, the apparent disparity between optical and molecular outflow velocities could be explained if the optical flow is much less massive than the molecular outflow (which is what is expected). In addition, it could be that the HH object originally had a larger velocity (the usual 100–200 km s$^{-1}$), but it has decelerated as it interacts with the ambient medium to velocities closer to 30–50 km s$^{-1}$—much like the giant HH flow HH 34 (Devine et al. 1997; Cabrit & Raga 2000). If such is the case, then the apparent disparity between optical and CO outflow velocity would be much less (almost negligible). We will not be sure of the exact kinematics of HH 315C until spectra and proper motions are measured for this optical knot. Independent of the kinematics of the HH 315C optical knot, what is really important to the discussion of this paper is that the morphology of the outflowing molecular gas in the hh315b+c region, along with other factors discussed below, strongly suggests that the molecular outflow is bow shock driven.

In Figure 3j we show the $^{12}$CO (2–1) integrated over the velocities between 1.01 and 1.89 km s$^{-1}$. The ambient cloud velocity in this region is 1.5 km s$^{-1}$ (see Paper I), and so most of the " ambient " cloud is found at this velocity range. In Figure 3k we plot the $^{12}$CO (2–1) integrated over the velocities between 1.89 and 2.55 km s$^{-1}$. This velocity range also includes emission from ambient cloud gas, since the gas emission shows an extended, cloudlike, morphology. In both Figures 3j and 3k, the density gradient of the cloud is clearly seen; the cloud's edge is in the east, and the density increases toward the west. At these ambient velocities, there is an increase in the column density at the position of the different small knots that comprise the HH 315C knot. In addition, the $^{12}$CO (2–1) contours near the HH 315C knots curve, following the bowlike configuration of the optical knots. Thus, we see that the HH 315C CO shell structure is also detectable at ambient cloud velocities—evidence that the HH 315 flow has altered the ambient gas distribution at distances as far as $\sim$1.5 pc from the source (see Paper I for more on this).

The $^{12}$CO (2–1) map integrated over the range of 2.55 km s$^{-1}$ < $v$ < 3.65 km s$^{-1}$ (Fig. 3l), which is redshifted with

respect to the ambient cloud velocity of the region, shows a " clump " of emission coincident with the HH 315C optical knot. Similar to what is seen in the other (blueshifted) velocity-integrated maps in Figure 3, the $^{12}$CO (2–1) intensity contours curve, following the bowlike arrangement of the HH 315C optical knots. This redshifted emission is presumably outflowing gas accelerated by the " back side " of the shock front associated with HH 315C.

In Figure 4 we show several sample $^{12}$CO (2–1) spectra from the hh315b+c region. It is interesting to note the drastic differences between spectra from regions very close to each other. Also, notice that the outflow emission is not a smooth low-level wing at blueshifted velocities. Instead, it is made of different velocity (spectral) components, which sometimes are stronger than the ambient cloud component.

### 3.1.2. $^{13}$CO Emission

The $^{13}$CO emission in the HH315b+c region has less complicated velocity structure than the $^{12}$CO emission. Similar to what is observed in the large-scale map (see Fig. 3 in Paper I), the $^{13}$CO (1–0) emission at velocities greater than 1.5 km s$^{-1}$ in this region is very weak ($T_{mb} \lesssim 0.6$ K), and hence most of the $^{13}$CO emission in this region is blueshifted compared to the cloud's ambient velocity. In Figure 5 we show three different $^{13}$CO velocity-integrated intensity maps. The different ranges of integration were chosen to group different channels with similar $^{13}$CO (1–0) emission structure.

The $^{13}$CO vaguely follows the $^{12}$CO bow shock structure associated with HH 315C. Both the north and the south bow shock wings are clearly present in $^{13}$CO emission, yet there is very little $^{13}$CO emission at the location of the bow shock apex. The north and south $^{13}$CO bow wings are spatially coincident with the $^{12}$CO bow wings with similar velocities. We do not detect any $^{13}$CO emission associated with the high-velocity gas surrounding the HH 315B knot. The structure of the high spatial resolution $^{13}$CO is consistent with our original hypothesis (Paper I) that the blueshifted northern lobe of the HH 315 molecular outflow has " pushed " aside gas, creating a shell-like structure at its edges, which is dense enough ($n \gtrsim 500$ cm$^{-3}$) that it is detected in $^{13}$CO (1-0) emission.

### 3.1.3. Mass

In Table 3 we list the mass for each of the velocity ranges shown in Figure 3. The mass was obtained using our high-resolution (IRAM 30 m) $^{12}$CO (1–0) and $^{13}$CO (1–0) data, with the procedure described in Paper I. The only difference in the procedure is the use of the average excitation temperature ($\bar{T}_{ex}$), given in Table 3, to estimate the outflow mass of a given velocity range (rather than using $T_{ex} = 10.5$ K for all velocities). Notice that the mass of the ambient cloud velocity range (1.01 km s$^{-1}$ < $v$ < 2.55 km s$^{-1}$) is approximately the same as the sum of the rest of the velocity ranges. This implies that in this region the outflow mass is approximately the ambient cloud mass. We first noticed this with our large-scale CO maps (Paper I), and its importance is discussed there.

### 3.2. The Region Surrounding HH 215 and PV Cep

The other region studied at high resolution with the IRAM 30 m telescope is the area surrounding the outflow source, PV Cep. This area is where most of the southern
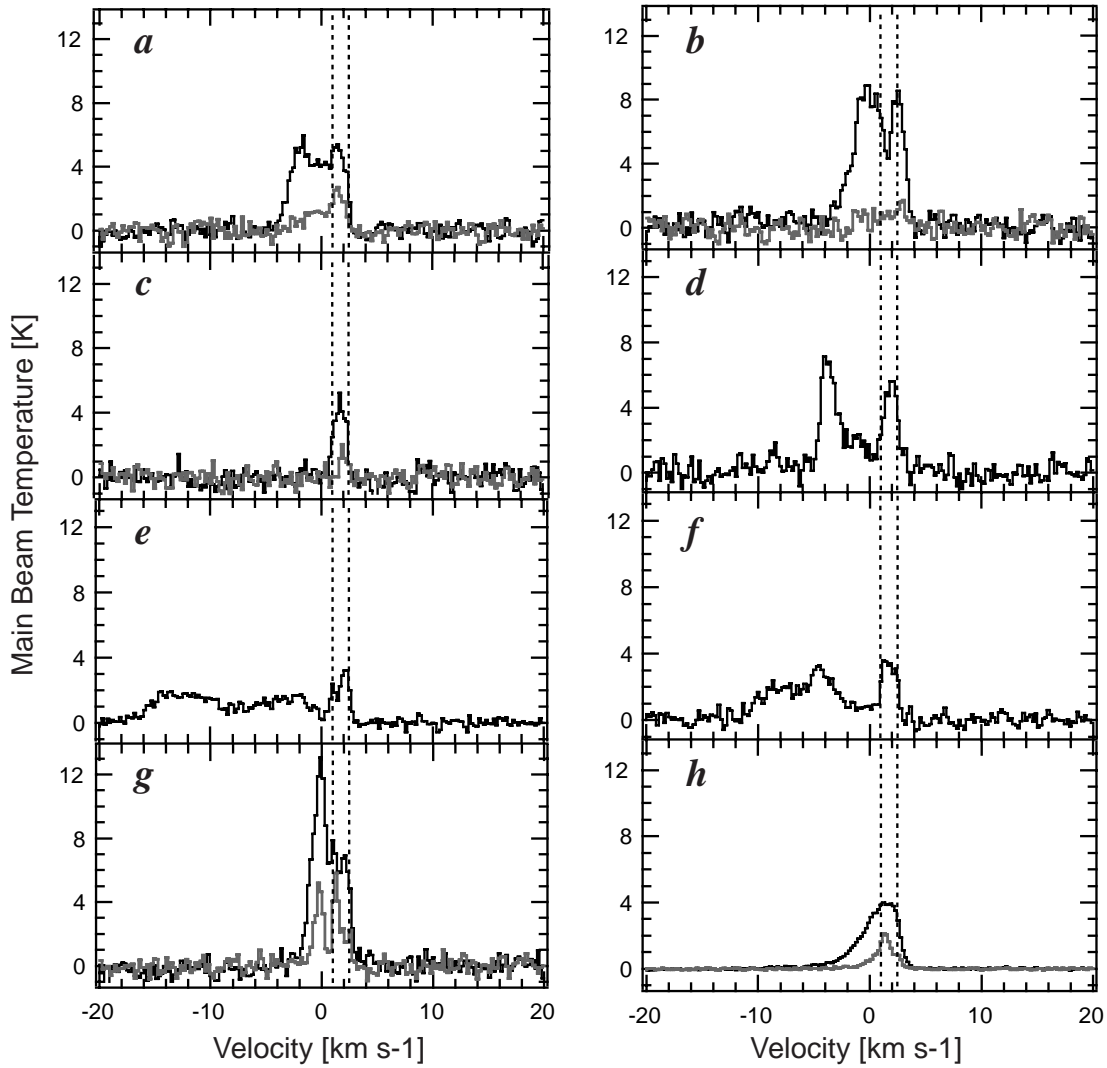
---

[2] Most, but not all, HH objects have been found to have velocities between 100 and 200 km s$^{-1}$ (Hartigan et al. 2000; Reipurth & Bally 2001).

Fig. 4.—Sample $^{12}CO$ (2–1) (*black*) and $^{13}CO$ (1–0) (*gray*) spectra of the hh315b+c region. Panels *a–g* show spectra from the position shown in Fig. 3*g*. Each spectrum (*a–g*) was taken from a single $10\rlap{.}{''}5 \times 10\rlap{.}{''}5$ pixel of a molecular-line map convolved with a 21″ beam. Panel *h* shows the average spectra over the whole hh315b+c region. The dotted vertical lines indicate the approximate range of the ambient cloud velocities (1.0 km s$^{-1}$ < v < 2.5 km s$^{-1}$) in the hh315b+c region.
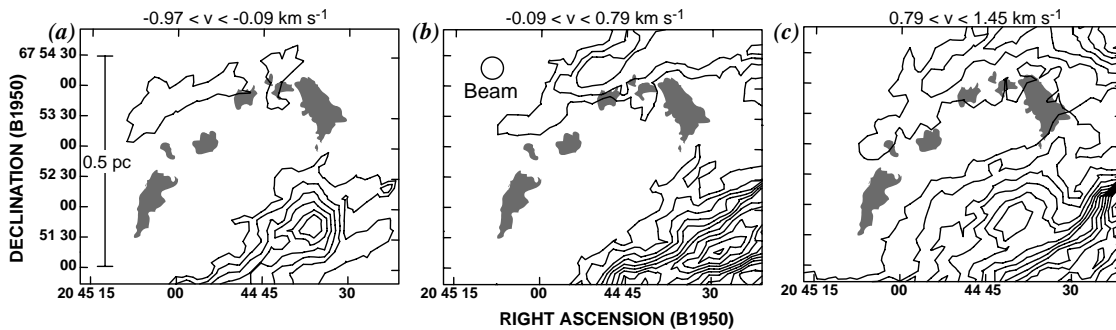


Fig. 5.—Velocity-range–integrated intensity maps of the $^{13}CO$ (1–0) emission surrounding the blueshifted optical knots HH 315C and HH 315B. The velocity range of integration is shown at the top of each panel. The gray silhouettes represent the S [II] knots in the region; see Fig. 3. All panels have the same starting contour and contour step value of 0.18 K km s$^{-1}$. The linear scale is shown in panel *a*, and the IRAM 30 m beam at the $^{13}CO$ (1–0) frequency (22″) is shown in panel *b*.

TABLE 3

Mass at Different Velocity Ranges in hh315b+c

| Velocity Range[a] (km s$^{-1}$) | $\bar{T}_{ex}$[b] (K) | Mass ($M_\odot$) | Momentum[c] ($M_\odot$ km s$^{-1}$) | Kinetic Energy[c] ($10^{43}$ ergs) |
|---|---|---|---|---|
| $-15.27 < v < -10.43$........ | 21.7 | 0.01 | 0.14 | 1.94 |
| $-10.43 < v < -6.03$.......... | 18.6 | 0.03 | 0.25 | 2.27 |
| $-6.03 < v < -3.39$ ........... | 17.8 | 0.05 | 0.30 | 1.76 |
| $-3.39 < v < -2.29$ ........... | 15.4 | 0.07 | 0.30 | 1.26 |
| $-2.29 < v < -1.19$ ........... | 13.0 | 0.17 | 0.53 | 1.64 |
| $-1.19 < v < -0.09$ ........... | 11.0 | 0.76 | 1.52 | 3.10 |
| $-0.09 < v < 1.01$ .............. | 10.5 | 2.88 | 2.65 | 2.69 |
| $1.01 < v < 1.89$[d]................ | 10.5 | 3.92 | . . . | . . . |
| $1.89 < v < 2.55$[d]................ | 10.5 | 1.31 | . . . | . . . |
| $2.55 < v < 3.65$ ................ | 10.5 | 0.58 | 0.77 | 1.08 |

[a] Velocity ranges are the same ranges as the ones in Fig. 3.

[b] Average excitation temperature at the given velocity range, using eq. (1), except for last four rows, where $\bar{T}_{ex} = 10.5$ (from Paper I).

[c] Radial component only. Value not corrected for the inclination angle ($i$) of the outflow axis with respect to the plane of the sky. If correction is to be done, we recommend $i \sim 10°$.

[d] Ambient cloud velocity range.

(redshifted) outflow resides (see Fig. 2). In addition, the area observed also covers the area north of PV Cep where the chain of five optical knots that make up HH 215 have been detected (GKW). We call this whole area the hh215 region. We note that in this region, the central ambient cloud velocity is $v_{amb, south} = 2.5$ km s$^{-1}$ (see Paper I), and so outflow velocities in the hh215 region are defined as the observed velocity minus 2.5 km s$^{-1}$.

### 3.2.1. $^{12}$CO (2–1) Emission

In Figure 6 we show the integrated intensity, over four different velocity ranges, of the $^{12}$CO (2–1) in the hh215 region. Notice that not all velocity integration ranges have the same width. The different ranges of integration were chosen to group different velocity (spectral) channels with similar $^{12}$CO (2–1) emission structure.

The most blueshifted velocity range in which we detect $^{12}$CO (2–1) emission in this region is shown in Figure 6a. The blueshifted molecular outflow emission in this velocity range ($-0.15$ km s$^{-1}$ $< v <$ 0.74 km s$^{-1}$) is concentrated at the source and north of it. The emission detected south (and southeast) of the source in Figure 6a is from another cloud in the same line of sight (cloud X) that we detect in our large-scale $^{12}$CO and $^{13}$CO maps (see Figs. 2 and 3 in Paper I). The blueshifted $^{12}$CO (2–1) outflow emission in Figure 6a is very poorly collimated—unlike the outflowing redshifted emission discussed below—nor does it show the nice bow shock structure observed in the hh315b+c region.

In Figure 6b we show the (blueshifted) $^{12}$CO (2–1) integrated emission over the velocity range between 1.62 km s$^{-1}$ $< v <$ 2.06 km s$^{-1}$. We do not include an integrated velocity map for velocities between 0.74 and 1.62 km s$^{-1}$, since at these velocities the $^{12}$CO is dominated by the emission from cloud X all through the mapped region and so no outflow features are observed. The velocity range in Figure 6b includes velocities as close as $\sim$0.5 km s$^{-1}$ to the central ambient velocity of 2.5 km s$^{-1}$, so there is some ambient cloud emission contribution to the $^{12}$CO (2–1) emission at these velocities. The contours were chosen to show the brightest features. It can be seen that the emission peaks

near the position of PV Cep and extends north with a fanlike structure (with an opening angle of $\sim$90°). This wide-angle structure does not resemble any cloud structure observed in our large-scale maps. Thus, we believe that the emission north of PV Cep in Figure 6b comes from the slowest, detectable (blueshifted) outflow emission in the hh215 region. This slow outflow gas has a morphology that is consistent with it being entrained by a wide-angle wind. We further discuss this in § 4.3.3.

The emission south of PV Cep in Figure 6b is ambient cloud emission, which we easily identify with a structure seen in our large-scale maps. Notice that this emission south of PV Cep in Figure 6b delineates the walls of the cavity cleared by the redshifted outflow lobe (Figs. 6c and 6d). This cavity is also observed in our large-scale map, and we discuss its importance in Paper I.

Between velocities 2.06 and 3.16 km s$^{-1}$, the detected $^{12}$CO (2–1) comes from (extremely optically thick) ambient emission, which shows no (or very little) structure. The slowest detectable redshifted outflow emission is at $v \sim 3.2$ km s$^{-1}$, and it is easily identified as outflow gas from the obvious non-cloudlike morphology of the gas emission.

The redshifted outflow gas shows a very peculiar structure, very different from the wide-angle blueshifted outflow emission discussed above. At the lowest redshifted velocities (Fig. 6c) the $^{12}$CO (2–1) integrated intensity peaks at the position of PV Cep and has a cometary-like extension toward the east and a collimated (jetlike) extension toward the south. The east-west cometary-like structure is clearly detected only at the velocities between $\sim$3.2 and 5.2 km s$^{-1}$ and extends farther than the eastern limits of our map. We believe that this cometary-like structure is associated with the motion of PV Cep through the cloud (see A. A. Goodman & H. G. Arce 2002, in preparation). The north-south structure seen in Figure 6c extends about 1.75 ($\sim$0.25 pc) and resembles a curving (or wiggling) CO jet, with an eastward bent at $\sim$1′ south of PV Cep.

At high (redshifted) outflow velocities (see Fig. 6d) we detect a north-south $^{12}$CO structure similar to the one seen in Figure 6c. About 50″–60″ south of PV Cep there is a "bump," where the collimated north-south structure
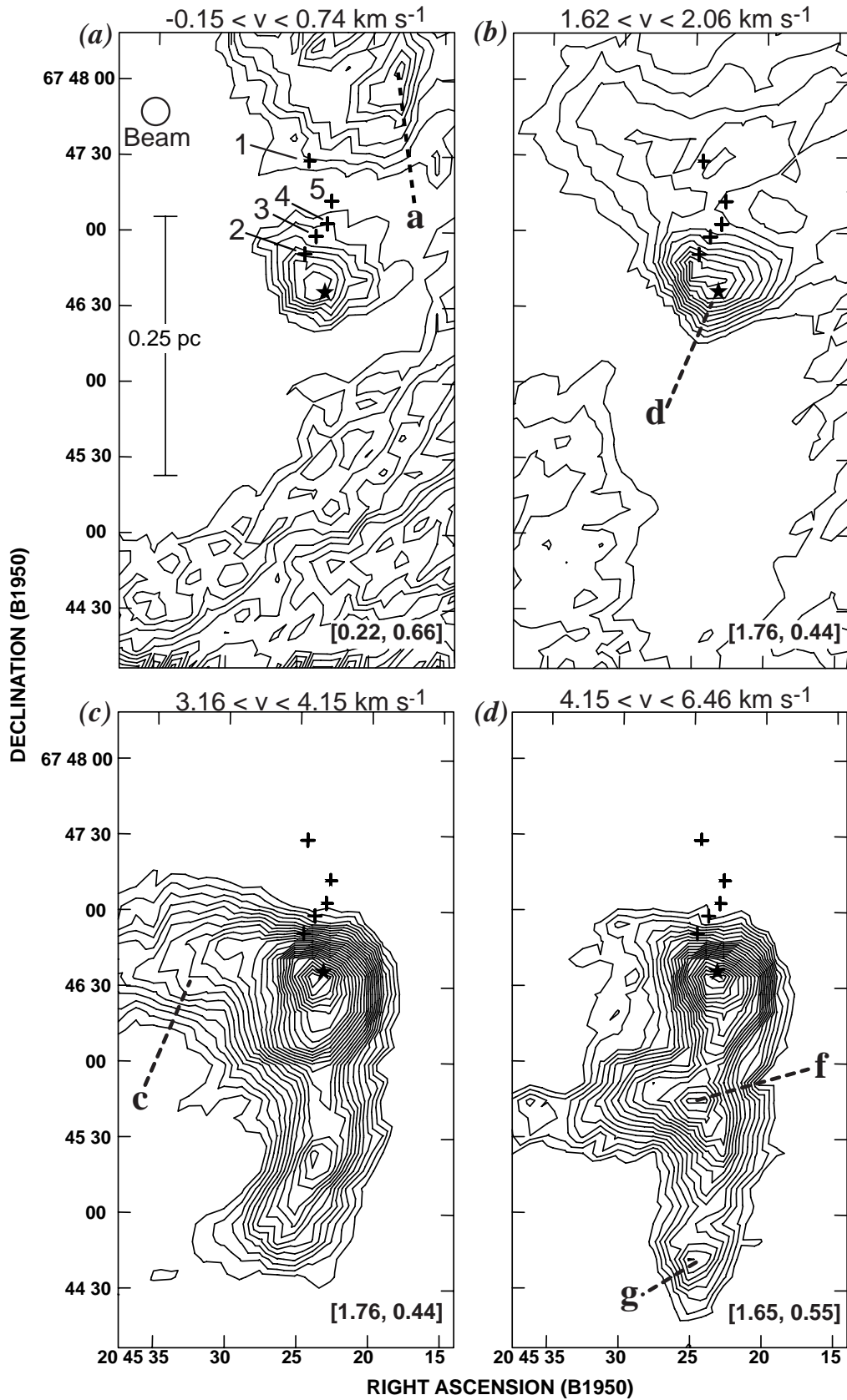
FIG. 6.—Velocity-range–integrated intensity maps of the $^{12}$CO (2–1) emission surrounding PV Cep, HH 215, and the southern redshifted outflow lobe (i.e., the hh215 region; see Fig. 2). The velocity range of integration is shown at the top of each panel. The starting contour and the contour steps are given in brackets at the lower right corner of each panel in units of K km s$^{-1}$. The star symbol denotes the position of the outflow source, PV Cep, and the plus signs denote the position of the different HH 215 knots 1–5 (from GKW), identified in panel $a$. The IRAM 30 m beam at the $^{12}$CO (2–1) frequency is also shown in panel $a$. The letter inside the panels identify the position from which we obtain the spectra shown in Fig. 9. Each letter represents the position of the spectrum shown in the panel (in Fig. 9) with the same letter.
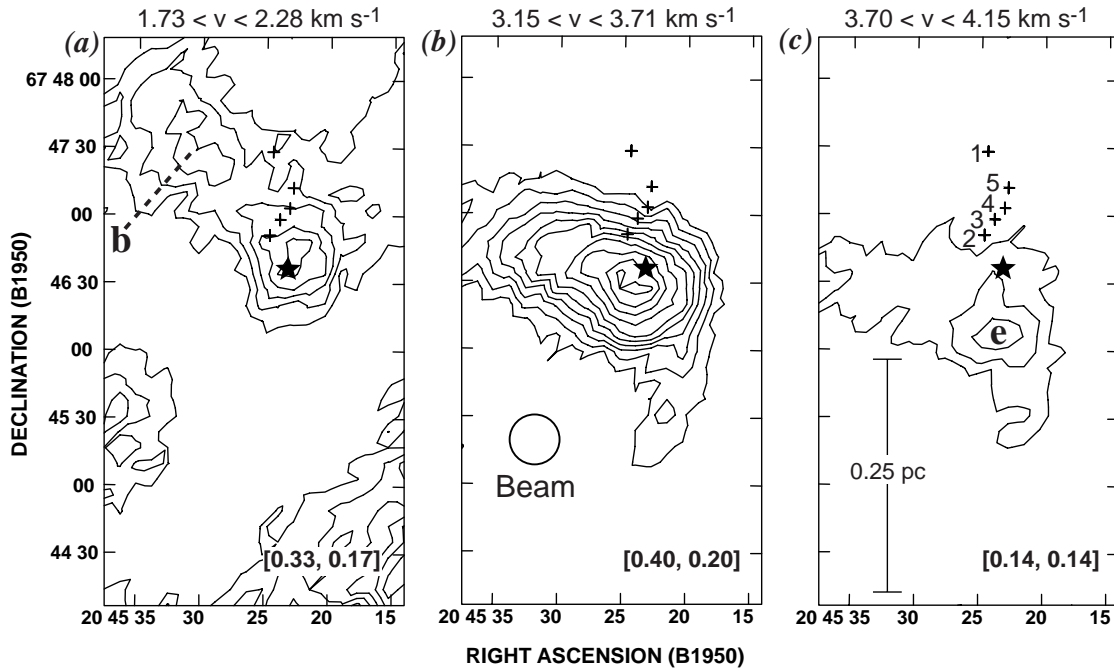
Fig. 7.—Velocity-range–integrated intensity maps of the $^{13}$CO (1–0) emission in the hh215 region. The velocity range of integration is shown at the top of each panel. The starting contour and the contour steps are given in brackets at the lower right corner of each panel in units of K km s$^{-1}$. The star symbol denotes the position of the outflow source, PV Cep, and the plus signs denote the position of the different HH 215 knots 1–5 (from GKW), identified in panel c. The IRAM 30 m beam at the $^{13}$CO (1–0) frequency is shown in panel b. The letters inside the panels identify the position from which we obtain the spectra shown in Fig. 9. Each letter represents the position of the spectrum shown in the panel (in Fig. 9) with the same letter.

widens. As discussed later (§ 4.3.2), this bump is most probably due to the entrainment of the ambient gas by a redshifted counterepisode of HH 215. South of the bump the jetlike structure continues, and it ends about 2′ (∼0.29 pc) south of PV Cep, slightly further south than the north-south structure in Figure 6c.

### 3.2.2. $^{13}$CO Emission

In Figure 7 we show three different velocity-integrated intensity maps of the $^{13}$CO (1–0) emission in the hh215 area. Similar to the other velocity-integrated maps presented here, the ranges of integration were chosen to group different velocity (spectral) channels with similar $^{13}$CO (1–0) emission structure.

Figure 7a shows the most blueshifted $^{13}$CO emission in the hh215 area, at velocities between 1.73 and 2.28 km s$^{-1}$. The velocity range is very narrow (only 0.55 km s$^{-1}$ wide), and the velocities are close to the central ambient gas velocity (2.5 km s$^{-1}$). The blueshifted $^{13}$CO integrated intensity map (Fig. 7a) shows a clear V-shaped structure with its apex at the position of PV Cep. As shown in Figure 8, this $^{13}$CO structure is coincident with the optical reflection nebula north of PV Cep (Cohen et al. 1981; Gledhill, Warren-Smith, & Scarrot 1987; Levreault & Opal 1987; Neckel et al. 1987; Scarrot, Rolph, & Tadhunter 1991; Reipurth, Bally, & Devine 1997a, hereafter RBD; GKW) and encloses the wide-angle $^{12}$CO (2–1) blueshifted outflow seen in Figure 6b. Thus, it appears that $^{13}$CO in this velocity range traces the limb-brightened walls of a wind-blown cavity. We discuss this further in § 4.3.3.

The other two velocity-integrated intensity maps of $^{13}$CO (1–0) (Figs. 7b and 7c) come from redshifted velocities (compared to the ambient cloud velocity of 2.5 km s$^{-1}$). The

$^{13}$CO integrated intensity emission in Figure 7b resembles (and coincides with) the east-west cometary-like structure in the $^{12}$CO (2–1) integrated intensity map in Figure 6c. In addition to the east-west structure, there is a low-emission north-south elongation, which partly coincides with the north-south $^{12}$CO (2–1) jetlike structure in Figure 6c and extends only ∼1′3 (0.18 pc) south of PV Cep. Figure 7c shows the most redshifted $^{13}$CO emission in the hh215 region. At these velocities the $^{13}$CO emission is very weak compared to the other velocities shown, and the maximum emission is just south of PV Cep.

In Table 4 we list the mass for each of the velocity ranges shown in Figure 6. The mass was obtained using our IRAM 30 m $^{12}$CO (1–0) and $^{13}$CO (1–0) data, using the procedure described in Paper I (with $T_{ex} = 10.5$ K for all velocity ranges). In Figure 9 we show sample $^{12}$CO (2–1) and $^{13}$CO (1–0) spectra from the hh215 region.

TABLE 4
Mass at Different Velocity Ranges in hh215

| Velocity Range[a] (km s$^{-1}$) | Mass ($M_\odot$) | Momentum[b] ($M_\odot$ km s$^{-1}$) | Kinetic Energy[b] ($10^{43}$ ergs) |
|---|---|---|---|
| $-0.15 < v < 0.74$ ....... | 0.01 | 0.03 | 0.06 |
| $1.62 < v < 2.06$ .......... | 0.94 | 0.43 | 0.23 |
| $3.16 < v < 4.15$ .......... | 1.31 | 1.25 | 1.28 |
| $4.15 < v < 6.46$ .......... | 0.27 | 0.30 | 1.51 |

[a] Velocity ranges are the same ranges as the ones in Fig. 6.
[b] Radial component only. Value not corrected for the inclination angle ($i$) of the outflow axis with respect to the plane of the sky. If correction is to be done, we recommend $i \sim 10°$.
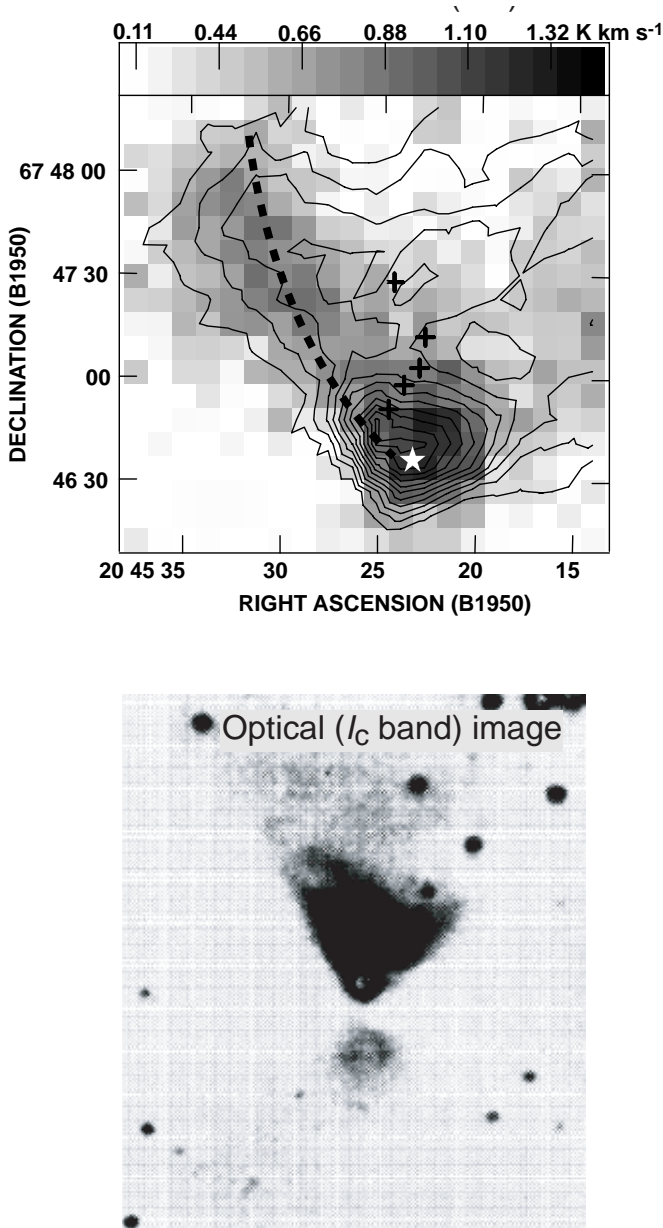
Optical ($I_c$ band) image

FIG. 8.—*Top panel*: Velocity-range–integrated intensity contour map of blueshifted $^{12}$CO (2–1) emission (within 0.3 pc north of PV Cep in hh215 region) superimposed on gray-scale map of blueshifted $^{13}$CO (1–0) emission of the same area. The velocity range of integration and the contours of the $^{12}$CO (2–1) map are the same as Fig. 6b, and the gray-scale map comes from Fig. 7a. The star and plus signs show the same as previous figures. The dashed dark line represents the eastern edge of the optical nebula north of PV Cep. *Bottom panel*: $I_c$ image of the PV Cep biconical nebulosity (from Levreault & Opal 1987). The field shown is 2′.58 high.

### 3.3. *The Region Surrounding HH 315E*

The sensitivity of our observations in the hh315e region is similar to that of the other regions (see Table 2). So, if the column density of the outflowing CO gas in the hh315e region were similar to that of the other regions, then outflowing CO should be easily detectable. But, even though HH 315E is the counterknot of HH 315B—where we detect CO with the highest blueshifted outflow velocities—we do not detect any outflow emission in the region surrounding the optical knot HH 315E.

In Figure 10 we show an average $^{12}$CO (2–1) spectrum of the hh315e region. The spectrum does not show any redshifted low-level wing, or another velocity component redshifted from the ambient emission, as might be expected for a redshifted CO outflow lobe spectrum. Instead, the spectrum shows mainly ambient gas emission from the cloud associated with PV Cep (the "PV Cep cloud"), which peaks at $v \sim 2.5$ km s$^{-1}$ (see Paper I). The bump in the spectrum seen at blueshifted velocities is due to "contaminating" emission from another cloud in the same line of sight. We fit a double Gaussian to the average spectrum, and from the fit we obtain that the PV Cep cloud component (centered at $\sim 2.5$ km s$^{-1}$) has a width (FWHM) of $\sim 0.8$ km s$^{-1}$. Even if we fit a single Gaussian, the resultant velocity width is 1.1 km s$^{-1}$.

A $^{12}$CO (2–1) spectrum with such a narrow velocity is usually observed in quiescent ambient gas clouds rather than in regions affected by stellar outflows. HH knots are shocks arising from the interaction of a high-velocity flow of gas ejected by a young stellar object and the ambient medium. Thus, we know that the outflow mass ejection responsible for the HH 315E optical knot is interacting with its surrounding medium because HH 315E is detected. It is strange that even though the column density of the ambient (molecular) gas in the hh315e region is more than the column density of the ambient (molecular) gas surrounding HH 315B, we see no evidence of outflow-cloud interaction in our CO spectra. One possible explanation is that the relatively high CO column density observed is all (or mostly) due to CO in front of HH 315E and that HH 315E is interacting only with atomic gas *behind* the PV Cep cloud.

## 4. ANALYSIS AND DISCUSSION

### 4.1. *Temperature Distribution*

We use our $^{12}$CO (1–0) and $^{12}$CO (2–1) data in concert to study the excitation temperature ($T_{ex}$) across the mapped regions. We then use the estimate of the temperature variations in our map to discern between different molecular outflow entrainment models. Since estimating the excitation temperature of optically thick ($\tau > 1$) gas is very unreliable (see, e.g., Fig. 5 in Hatchell, Fuller, & Ladd 1999), we will try to estimate the excitation temperature only of optically thin ($\tau < 1$) CO gas. And so, to obtain our temperature estimates, we will use the optically thin approximation and the following equation (Bachiller & Tafalla 1999):

$$R_{21/10} = 4e^{-11/T_{ex}}, \qquad (1)$$

where $R_{21/10}$ is the $^{12}$CO (2–1) to $^{12}$CO (1–0) line ratio.

We warn that equation (1) is only exact in the optically thin limit ($\tau \ll 1$). Using equation (1) with gas with an opacity as low as $\tau \sim 0.1$ would lead to an underestimation of the real excitation temperature. If $\tau \sim 0.1$, the discrepancy stays within 20% for CO line ratios lower than 2.5, but for line ratios higher than 2.8, the error in $T_{ex}$ exceeds 40%. In any case, it is still true that for any given opacity, the higher the line ratio, the higher the excitation temperature. So even though equation (1) does not give a perfect estimate for $\tau \gtrsim 0.01$, we can still use it to investigate the *relative* temperature distribution.
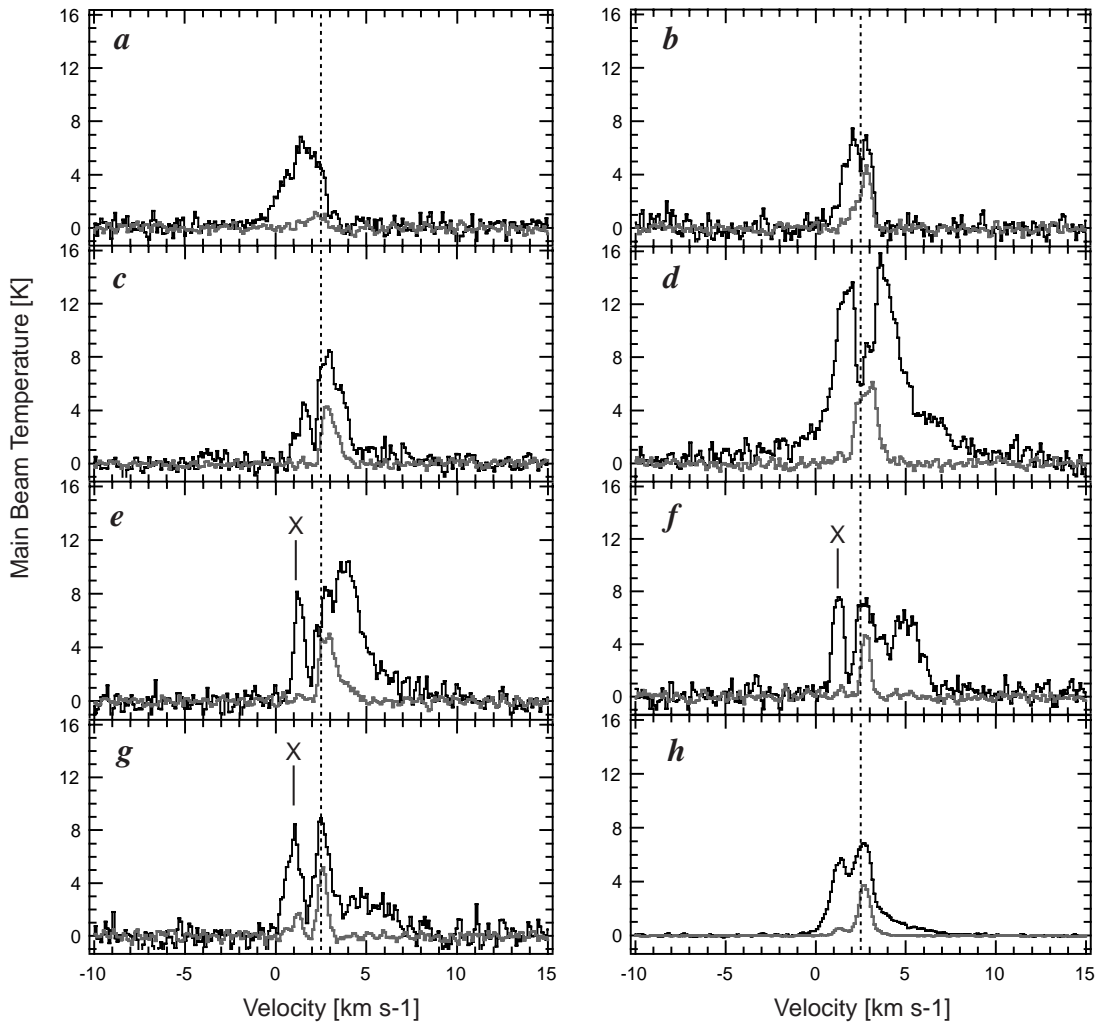
FIG. 9.—Sample $^{12}$CO (2–1) (black lines) and $^{13}$CO (1–0) (gray lines) spectra of the hh215 region. Panels a–g show spectra from the positions shown in Figs. 6 and 7. The spectra shown in panel d come from the position of the outflow source, PV Cep. Each spectrum (a–g) was taken from a single $7'' \times 7''$ pixel of a molecular-line map convolved with a $14''$ beam. In panel h we show the average spectra over the whole hh215 region. The dotted vertical line indicates the position of $v = 2.5$ km s$^{-1}$.
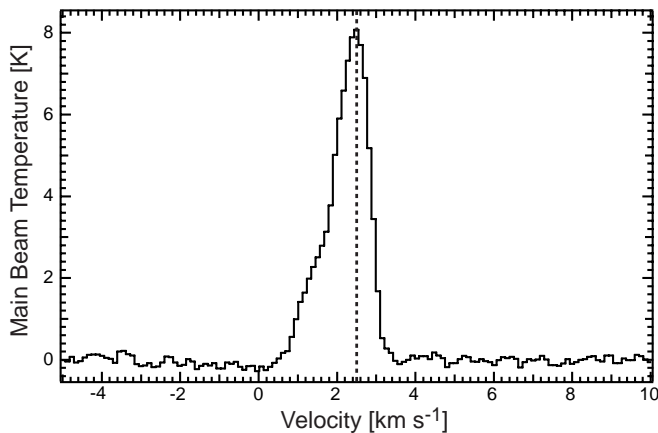


FIG. 10.—Average $^{12}$CO (2–1) spectrum of the mapped area surrounding the redshifted optical knot HH 315E (i.e., the hh315e region; see Fig. 2). A dashed line indicates the position of $v = 2.5$ km s$^{-1}$. The main component, with a peak in $T_{mb}$ at $v = 2.5$ km s$^{-1}$, is due to ambient gas from the cloud associated with PV Cep. The bump in the spectrum at blueshifted velocities is due to emission from another cloud in the same line of sight.

### 4.1.1. The hh315b+c Region

To estimate the excitation temperature of the outflow gas in the region surrounding the optical knots HH 315B and HH 315C, we used velocity-integrated maps of the $^{12}$CO (2–1) and $^{12}$CO (1–0) lines. For each velocity-integrated map, we produced a map of the line ratio ($R_{12/10}$) and then a map of the excitation temperature, using equation (1). Five gray-scale maps of $T_{ex}$ are shown in Figure 11 (the velocity ranges of integration are the same as Figs. 3b–3f). Gas with velocities close to the ambient velocity is optically thick, and so we do not obtain an estimate of $T_{ex}$ for gas at those velocities. For each gray-scale temperature map, we superimposed the $^{12}$CO (2–1) velocity-integrated intensity contours. We obtain a value of $T_{ex}$ only for pixels with an S/N of at least 5, in both $^{12}$CO (2–1) and $^{12}$CO (1–0). We masked (set $T_{ex} = 0$) the low-S/N pixels and those (few) that gave unphysical negative values of $T_{ex}$.

In all panels of Figure 11, there is a discernible trend in which there is a temperature increase in regions with high-velocity outflowing CO emission. That is, whereas $T_{ex} = 10.5$ K for ambient cloud velocities (see Paper I), $T_{ex} > 11$ K for outflowing gas. In addition, the average $T_{ex}$
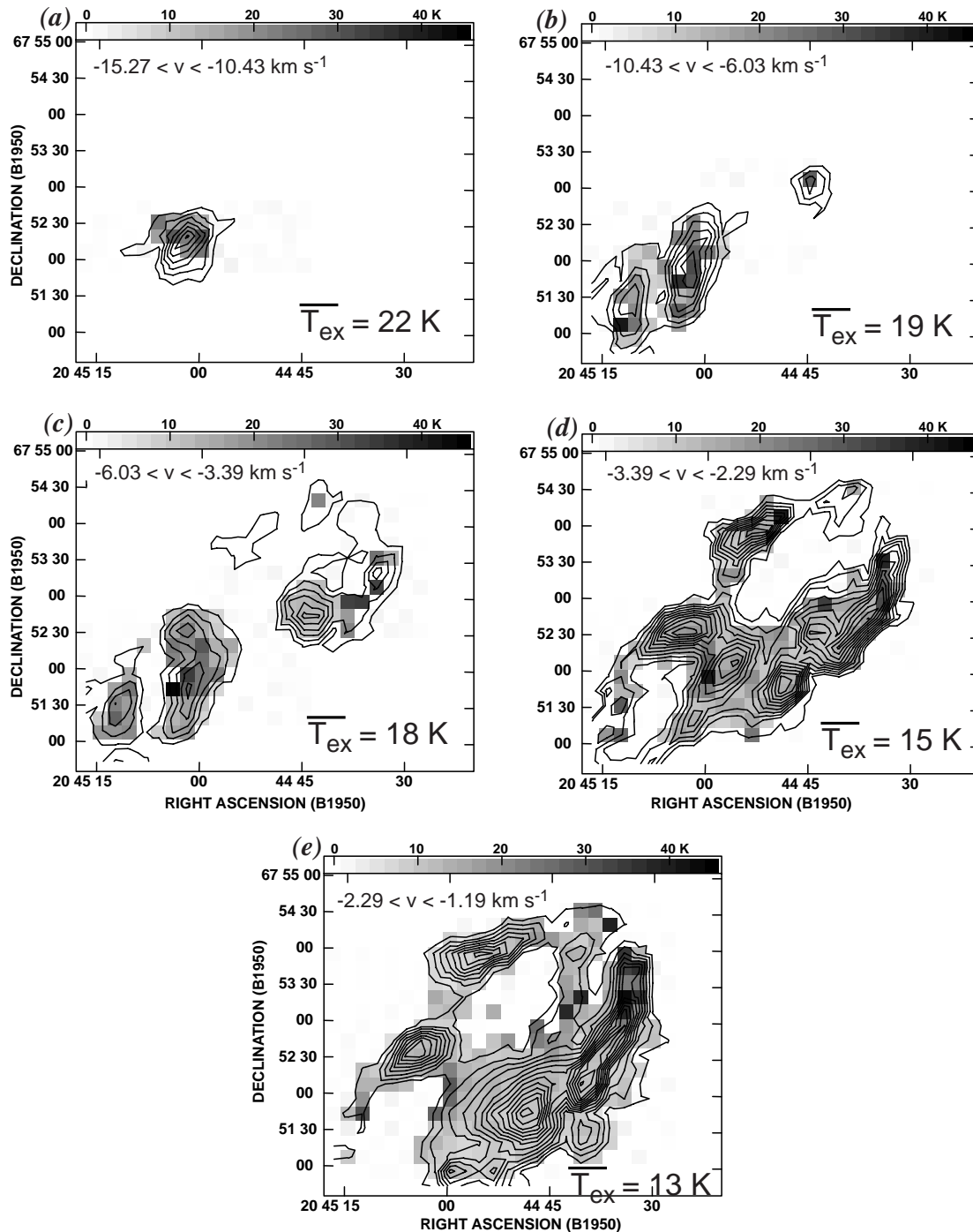
Fig. 11.—Gray-scale excitation temperature maps of the CO outflow gas in the hh315b+c region. Superimposed on the gray-scale maps, we show in contours the $^{12}CO$ (2–1) velocity-integrated intensity. The velocity range of integration is shown at the top of each panel. The first contour and contour steps for each panel are the same as for the corresponding velocity range in Fig. 3. The average excitation temperature ($\overline{T}_{ex}$) for each velocity range (from Table 3) is shown at the bottom right corner of each panel. Each pixel is $12'' \times 12''$.

increases with outflow velocity (see also Table 3). This temperature distribution is consistent with the temperature distribution expected for a molecular outflow formed by bow shock (prompt) entrainment. Analytical and numerical jet-driven bow shock models show that the temperature of the accelerated gas that forms the molecular outflow should be higher than the ambient gas. In addition, the temperature is also expected to rise with increasing outflow velocity (e.g., Hatchell et al. 1999; Lee et al. 2001).

It should be noted that the warmer outflowing gas observed does not come directly from the shock cooling length behind the shock front. Bow shock–driven outflow models predict that the outflowing gas is heated as a consequence of the acceleration (i.e., increase in kinetic energy) of the gas driven by the momentum-conserving interaction between the bow shock and the ambient medium (see Hatchell et al. 1999 for more on this). Another possible source of heating near an HH object may be the UV radia-
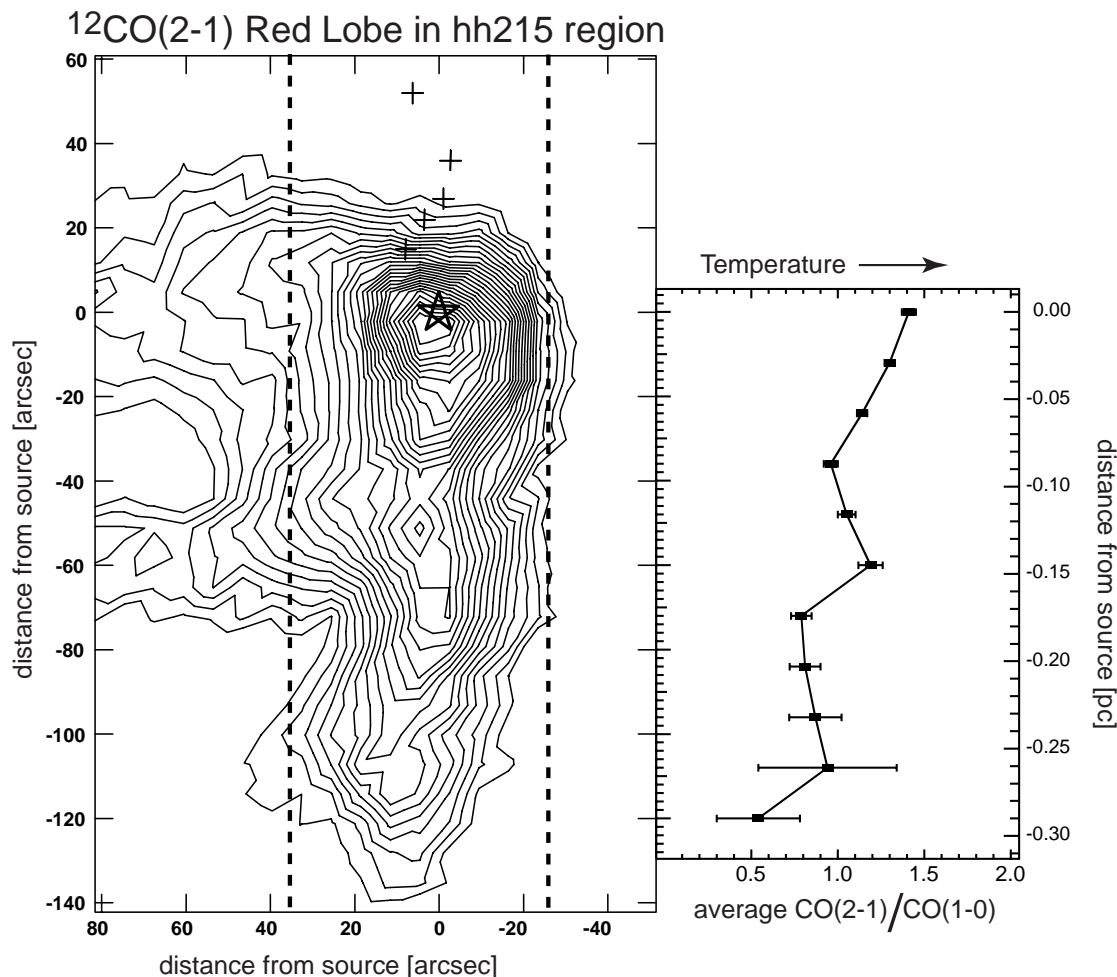
Fig. 12.—*Left panel*: $^{12}$CO (2–1) integrated intensity contours of the redshifted emission near PV Cep (hh215 region). The velocity range of integration is 3.16 km s$^{-1}$ < $v$ < 6.46 km s$^{-1}$. The starting contour and contour step are 2.64 and 0.88 K km s$^{-1}$, respectively. The star symbol indicates the position of PV Cep, and the plus signs indicate the position of the HH 215 knots. *Right panel*: Average $^{12}$CO (2–1) to $^{12}$CO (1–0) line ratio as a function of distance from the source. The line ratio is averaged over the width of the north-south jetlike structure, indicated by the dark vertical dashed lines on the left panel. The error bars indicate the 1 $\sigma$ error.

tion from the jet shock (see Wolfire & Königl 1993; Taylor & Williams 1996).

### 4.1.2. *The hh215 Region*

The $^{12}$CO gas detected (at most velocities) in the hh215 region is moderately optically thick ($\tau \sim 1$; see Paper I), and so estimates of the excitation temperature are very unreliable. Hence, we study the *relative* temperature distribution by studying the spatial distribution of the CO line ratio ($R_{21/10}$).

The map of the CO line ratio of the blueshifted outflow gas in the hh215 region does not show any significant structure and hence is not shown. The only clear trend in this map is that there is an increase in $R_{21/10}$ at the position of the source, implying there is an increase in temperature at the position of PV Cep.

In Figure 12 we plot the average line ratio along the axis of the redshifted molecular outflow lobe. To do this, we determine the average value of $R_{21/10}$ over the width of the jetlike outflow lobe, for each row of pixels, and then plot it as a function of declination offset from the source. The line ratio shown in Figure 12 has a maximum at the source posi-

tion, then it decreases with distance from the source up to about 36″ south of PV Cep. At about 60″ south of the outflow source position, $R_{21/10}$ reaches a local maximum. Farther south, along the outflow lobe axis, the CO line ratio stays approximately constant.

Models where the molecular outflow is formed by turbulent mixing of the ambient gas along the sides of a jet or wind predict that the gas temperature should have a maximum temperature at (Cantó & Raga 1991) or very close to (Lizano & Giovanardi 1995) the position of the source and decrease monotonically with distance from the source. Entrainment models where the gas is accelerated solely by the leading bow shock in a jet predict that the gas temperature should be minimum at the outflow source and increase toward the head of the bow shock, where the gas temperature peaks. Therefore, the gas temperature distribution implied by our measurements of $R_{21/10}$ is not entirely consistent with an outflow entrained by the leading jet bow shock or by a turbulent mixing layer along the sides of a jet.

One alternative explanation is that the outflow is entrained by a time-varying (pulsed) jet. A time-varying jet will have internal bow shocks (usually called internal working surfaces) along its axis (see, e.g., Raga et al. 1990; Stone

& Norman 1993b; Lee et al. 2001), and the gas temperature should increase at the head of each internal shock. Thus, each local increase in the CO line ratio could arise from the local increase in temperature expected at the head of each internal bow shock. In this picture, the increase in line ratio 60″ south of PV Cep could be due to the redshifted counter-knot of HH 215(1)—presumably also responsible for the bump in the integrated intensity of the redshifted molecular outflow lobe (see Fig. 12). We further discuss this in § 4.3.2. The increase in temperature at the source position could arise from an unresolved internal working surface very close to PV Cep.

### 4.2. Kinematics and Momentum Distribution

Studying the velocity and momentum distribution of the molecular outflow may help us distinguish between different entrainment models. It also helps us better understand how young stellar outflows interact with the ambient gas.

#### 4.2.1. Kinematics of the hh315b+c Region

In Figure 13 we show a $^{12}$CO (2–1) position-velocity ($p$-$v$) diagram of the hh315b+c region. This $p$-$v$ diagram was constructed by rotating our image of the hh315b+c region by $43°$ and summing the $^{12}$CO (2–1) spectra at each row of pixels.

Figure 13 clearly shows that the velocity peaks at the position of HH 315B and decreases toward the position of the source. This velocity distribution, where the velocity peaks at the shock head and decreases toward the outflow source, is consistent with models of bow shock–entrained molecular outflows. For these models such velocity structure is a natural consequence of the fact that the highest (radial) velocities are found at the head of the bow shock while the velocity decreases toward the wings.

Lee and coworkers' recent analytical (Lee et al. 2000) and numerical (Lee et al. 2001) studies show detailed $p$-$v$ diagrams of wide-angle wind driven molecular outflows. Their

results indicate that the $p$-$v$ diagrams of wide-angle wind driven molecular outflows have noticeable differences compared with the predicted $p$-$v$ diagram for bow shock–entrained molecular outflows (see Fig. 1 for a schematic illustration of this). We do not see any indication in Figure 13 of a structure similar to that shown in the $p$-$v$ diagrams of Lee et al. (2000, 2001) for wide-angle wind driven molecular outflows.

Figure 13 shows that the highest outflow velocities are at the head of the shock (i.e., HH 315B) and that the rise in velocity associated with HH 315B is restricted to a limited region of no more than 100″ ($\sim$0.2 pc). This indicates that most, if not all, of the entrainment is taking place at the head of the HH 315B shock. Thus, we totally discard turbulent entrainment along the sides of a jet (or wind) as the mechanism responsible for the outflowing gas associated with the HH 315B optical knot, and we suggest that bow shock entrainment is responsible instead.

North of HH 315B, there are two more local peaks in the velocity (see Fig. 13). Both of the velocity peaks come from outflowing gas associated with the HH 315C molecular bow structure. The northernmost local velocity peak is coincident with the brightest optical emission in HH 315C, which is also the head of the optical bow shock. The other local peak in velocity associated with HH 315C (at a distance of $\sim$100″ from HH 315B in Fig. 13) comes from outflow gas in the wings of the HH 315C CO bow (see Figs. 3c and 3d). As discussed above, a bow shock–entrained molecular outflow should have the peak velocity at the head of the shock, and *no* local peak in velocity is expected at the bow wings. The velocity structure of the outflowing gas associated with HH 315C does not resemble the velocity structure of a wide-angle wind driven molecular outflow either (see Lee et al. 2000, 2001). Turbulent entrainment is again discarded since the head of the shock does not show the slowest velocities in the outflow, as predicted by turbulent jet models. Although the kinematics of the molecular outflow associated with HH 315C are not entirely consistent with bow shock entrainment, other pieces of evidence presented here suggest that bow shock entrainment is still the best candidate (see § 4.3.1 for further discussion).

#### 4.2.2. Momentum Distribution in the hh315b+c Region

In order to study the momentum distribution of the blue-shifted outflowing gas surrounding HH 315B and HH315C, we constructed a momentum map of the region. The map was produced using the technique to estimate mass described in Paper I. With this method we obtain a map of the outflow mass for each position pixel and velocity channel $(x, y, v)$. We multiply the mass at each $(x, y, v)$ by the (radial) outflow velocity corresponding to the given velocity channel ($v_{out} = v - v_{amb, north}$) to obtain the line-of-sight (or radial) momentum at each pixel and channel. By integrating (summing) over velocity channels $[\sum m(x, y, v_i)v_{out,i} = P(x, y)]$, we obtain a momentum map over a given velocity range.

We stress that we are considering only the line-of-sight (or radial) component of the outflow momentum. In order to obtain the true momentum one needs to assume an inclination angle ($i$) between the flow's axis and the plane of the sky. By comparing the $p$-$v$ diagram of the hh315b+c region (Fig. 13) with the $p$-$v$ diagram of modeled bow shock–driven outflows (e.g., Lee et al. 2000, 2001; Smith et al. 1997), it
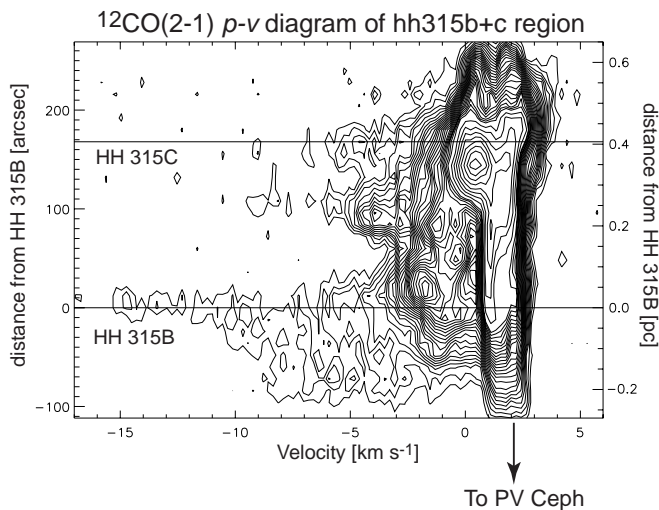


FIG. 13.—$^{12}$CO (2–1) $p$-$v$ diagram of the hh315b+c region. The $p$-$v$ diagram was constructed by rotating our $^{12}$CO (2–1) map of the hh315b+c region (with 12″ × 12″ pixels and 0.22 km s$^{-1}$–wide velocity channels) by $43°$ and summing the $^{12}$CO (2–1) spectra at each row of pixels. The horizontal lines denote the position of the brightest optical emission in the HH 315B and HH 315C knots. Contours are 3–51 K in steps of 2 K and 56–91 K in steps of 5 K.

appears that $0° < i < 30°$ in the hh315b+c region. In addition, the precession model of GKW estimates that HH 315 has an inclination to the plane of the sky of about $10°$. Thus, a value of $i \sim 10°$ seems adequate for HH 315. For the purpose of the entrainment mechanism studied in this paper, it is not important to correct the momentum by the inclination angle. However, if the true outflow momentum (and kinetic energy) is desired, we recommend that a value of $i \sim 10°$ should be used.

In Figure 14 we show the momentum map of the hh315b+c region, integrated over the velocity range $-15.27$ km s$^{-1}$ $< v < -0.09$ km s$^{-1}$. The bowlike structure of the outflowing gas associated with HH 315C is clearly seen in the momentum map. In this structure the bow wings show more momentum than the head of the bow. In addition, the southwestern wing has considerably more momentum than the northeastern bow wing. The maximum momentum in Figure 14 is nearly coincident with the brightest optical emission in HH 315B, and it is surrounded by a region of relatively high momentum extending south and extending east of the momentum peak. This extension traces the bow wings of the HH 315B CO bow shock, similar to what is seen in the HH 315C CO bow shock, but at a smaller scale.

In a bow shock–driven outflow model the outflowing gas velocity peaks at the head of the bow shock. The momentum ($p = mv$), on the other hand, is dependent on the underlying ambient cloud mass distribution (Chernin & Masson 1995). If a bow shock from a stellar wind mass ejection were to interact with an ambient gas with a perfectly uniform density distribution, the resultant molecular outflow momentum would peak at the head of the bow shock. This is not the case for HH 315C. As discussed in § 3.1, in this region there is a gradient in the ambient cloud density (seen in the ambient CO emission; see Figs. 3j and 3k), which increases from east to west. This explains why the southwest bow wing has more momentum than the northeast bow wings. Near both southwest and northeast bow wings the gas is denser than the gas at the head of the bow structure (we detect only $^{13}$CO emission near the HH 315C CO bow wings; see Fig. 5), thus the increase in momentum along the

bow wings with respect to the bow head. We conclude that the momentum distribution of the HH 315C molecular bow structure can be explained by the bow shock entrainment of ambient gas with a nonuniform density distribution.

The momentum distribution of the outflowing gas associated with HH 315B follows what is expected for a bow shock–entrained outflow in a relatively flat ambient density distribution. As can be seen in Figure 3, the outflowing gas associated with HH 315B is constrained to a small area surrounding HH 315B, and the ambient cloud density is approximately constant within that area. In Figure 14, the momentum peaks practically at the presumed bow shock head, and the momentum decreases away from the head, along the wings, toward the direction of the outflow source.

### 4.2.3. *Velocity Distribution in the hh215 Region*

Similar to hh315b+c, we studied the velocity distribution of the hh215 area by constructing a position-velocity diagram of the $^{12}$CO (2–1) emission. The *p-v* diagram, shown in Figure 15, was made by summing all spectra over the width of the hh215 area at each different row of pixels, resulting in a declination-velocity diagram.

There are several interesting features in the hh215 *p-v* diagram. The redshifted gas shows two distinctive velocity peaks; one is coincident with the position of PV Cep, and the other is $\sim 60''$ (0.15 pc) south of PV Cep. Most of the slow redshifted velocity coincident with the outflow source position comes from the east-west cometary-like structure seen in Figure 6c. We believe that most of this structure is a result of the motion of PV Cep through its parent cloud (see A. A. Goodman & H. G. Arce 2002, in preparation). So, most of the slow redshifted gas at the position of PV Cep is not related to the HH 315 outflow. Thus, we consider only the redshifted gas south of PV Cep as being part of the outflow.

The peak in velocity, $\sim 0.15$ pc south of PV Cep, is coincident (within the $11''$ beam of the telescope) with the "outflow clump" (or local maximum in the outflowing CO) south of PV Cep, seen in the $^{12}$CO (2–1) velocity-integrated map shown in Figure 6d. A peak in outflow velocity coincident with the position of an outflow clump has been attrib-
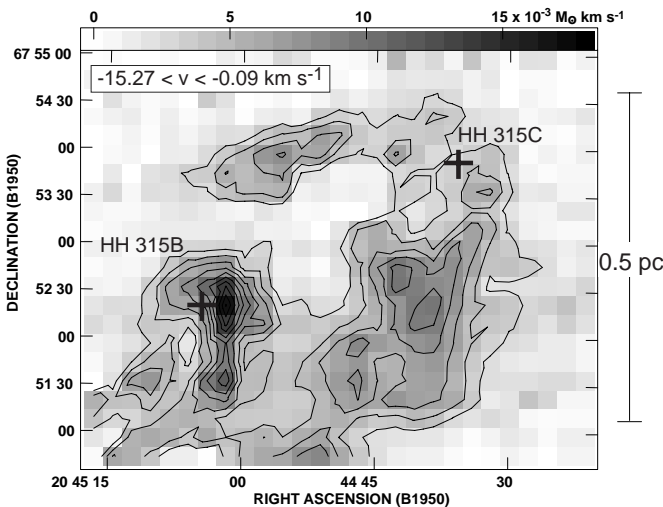


FIG. 14.—Map of the radial component of the molecular outflow gas momentum in the hh315b+c region, over the velocity range $-15.27$ km s$^{-1}$ $< v < -0.09$ km s$^{-1}$. The first contour and contour step are 3 and $1.5 \times 10^{-3}$ $M_\odot$ km s$^{-1}$, respectively. The plus signs denote the position of the brightest optical emission of the HH 315B and HH 315C knots.
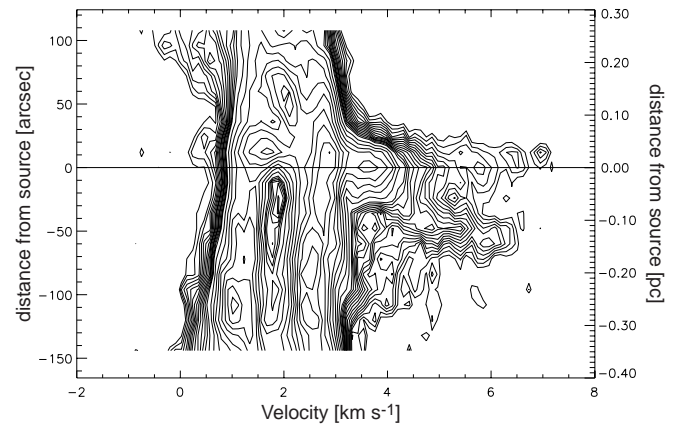


FIG. 15.—$^{12}$CO (2–1) *p-v* diagram of the hh215 region. The *p-v* diagram was constructed by summing all spectra over the width of the hh215 area at each different row of pixels, resulting in a declination-velocity diagram. The map used has $12'' \times 12''$ pixels and a velocity resolution of 0.11 km s$^{-1}$. The horizontal line indicates the position of the outflow source (PV Cep). Contours are 7–35 K in steps of 2 K and 40–80 K in steps of 5 K.

uted, in other outflows, to be evidence for bow shock (prompt) entrainment from a mass ejection episode (e.g., RNO 43, Bence et al. 1996; HH 300, Arce & Goodman 2001b).

We believe the optically undetected redshifted counterknots of the HH 215 chain of knots (see Fig. 6) are responsible for the entrainment of the redshifted outflow gas south of PV Cep. Each of the three major blueshifted knots of HH 315 (knots A, B, and C) have a redshifted counterknot (see Fig. 2), and for each of the three redshifted-blueshifted knot pairs, the distance from PV Cep to the blueshifted knot is the same (within 10%) as the distance from PV Cep to the corresponding redshifted counterknot (RBD). One would reasonably expect the same for the HH 215 knots, and so we believe that the rise in velocity ∼0.15 pc south of PV Cep is produced by the (unseen) counterknot of HH 215(1). It is very probable that optical observations have not detected HH knots in the corresponding location south of PV Cep because of the high extinction in this region.

As discussed in § 3.2, we detect a wide-angle blueshifted outflow emission north of PV Cep, in the hh215 region. In the p-v diagram (Fig. 15), the blueshifted gas shows a Hubble-like velocity distribution; the slowest blueshifted velocity (detached from the ambient cloud emission in the p-v diagram) is at ∼0.1 pc north of PV Cep, and the average blueshifted outflow velocity increases with distance from

the source, off our map limits (see Fig. 15). Given the limited coverage of the area, we cannot conclude if such velocity distribution is consistent with a bow shock–driven outflow model or a wide-angle wind driven molecular outflow model.

### 4.2.4. *Momentum Distribution in the hh215 Region*

As discussed in § 3.2, we are unable to estimate the total mass and momentum from the blueshifted outflow gas just north of PV Cep (in the hh215 region) because of contamination from the emission from another cloud in the same line of sight. This hinders our ability to compare the *total* blueshifted momentum with that expected by different entrainment models. Hence, we do not consider it here.

One the other hand, we can study the outflow momentum distribution of the redshifted lobe. In Figure 16, we plot the average momentum along the redshifted outflow axis, using a momentum map integrated over the velocity range of 3.16 km s$^{-1}$ < $v$ < 6.46 km s$^{-1}$. This plot was constructed by calculating the average momentum at each horizontal row of pixels along the north-south axis of the outflow and then plotting the average momentum as a function of distance from the source. In order to avoid redshifted emission not associated with the redshifted outflow lobe (i.e., the cometary-like east-west structure), we averaged the momentum



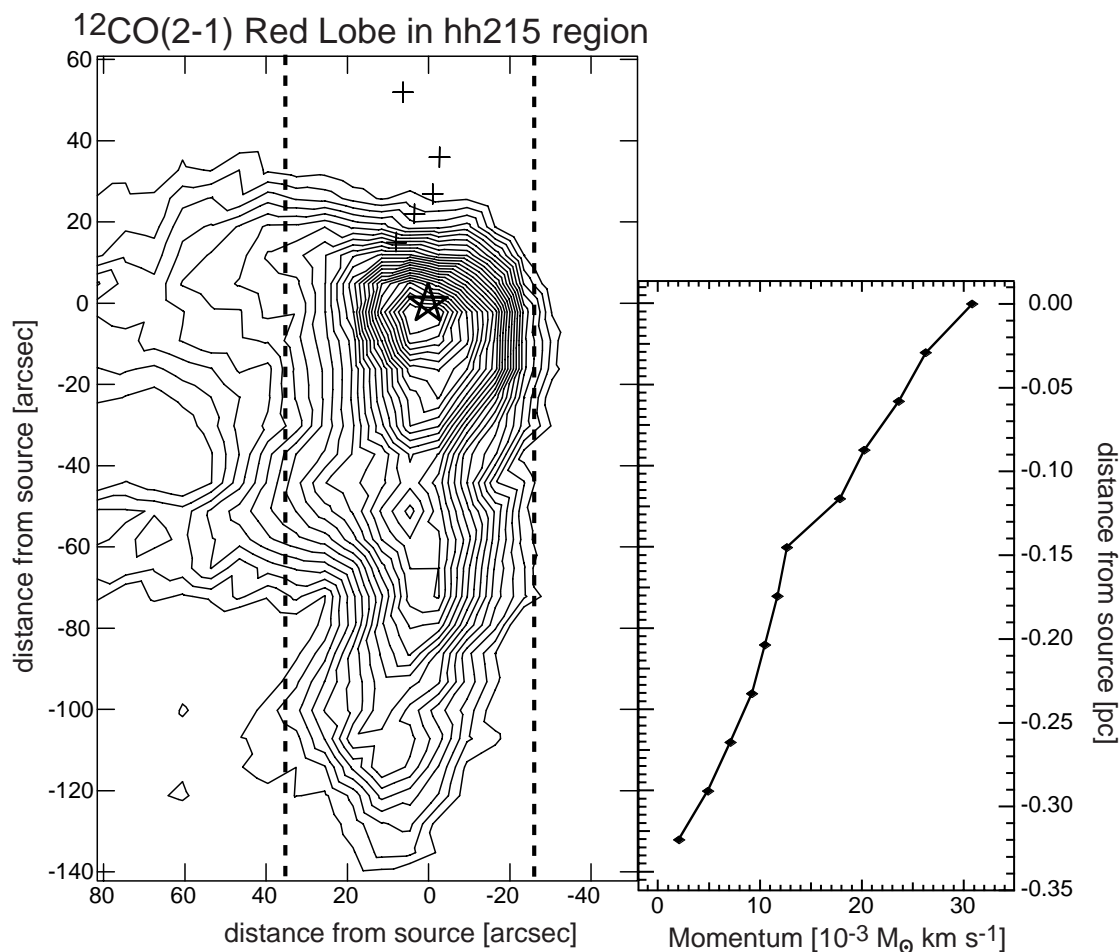$^{12}$CO(2-1) Red Lobe in hh215 region

FIG. 16.—*Left panel*: Same as left panel of Fig. 12. *Right panel*: Average momentum in the redshifted outflow lobe as a function of distance from PV Cep. The momentum was averaged over the width of the redshifted CO jetlike structure, indicated by the black vertical dashed lines on the left panel.

TABLE 5

COMPARISON OF MOLECULAR OUTFLOW ASSOCIATED WITH HH 315B AND RESULTS FROM ENTRAINMENT MODELS

| | | | CONSISTENT WITH MODEL? | | |
|---|---|---|---|---|---|
| PARAMETER | DESCRIPTION | FIGURE | Turbulent Jet | Bow Shock | Wide-Angle Wind |
| Morphology........ | Small bowlike, with wings extending in direction of outflow source | 3 | No | Yes | No |
| Temperature ....... | $T_{ex}$ of outflow greater than ambient $T_{ex}$, also increase in $T_{ex}$ with velocity | 11 | No | Yes | No |
| Velocity .............. | "Spurlike"—maximum velocity at position of HH 315B (shock head) | 13 | No | Yes | No |
| Momentum......... | Maximum at bow head | 14 | No | Yes | No |

over a restricted area, which includes only the north-south redshifted jetlike outflow structure (see Fig. 16). The average momentum along the redshifted lobe axis has a maximum at the source position, and it decreases with distance from the source. This momentum distribution is very similar to that predicted by Chernin & Masson (1995) for an outflow consisting of material swept-up by a jet bow shock traveling through an ambient cloud with a density gradient proportional to $r^{-a}$, where $1 \le a \le 2$. In this model the outflow momentum decreases with distance from the outflow source because the ambient cloud density decreases with distance from the young star. The ambient density of the PV Cep cloud (as implied by the integrated intensity $^{13}$CO maps of the cloud in Paper I) monotonically decreases with distance from PV Cep in the region where we detect the redshifted jetlike outflow feature. Therefore, the bow shock entrainment model of Chernin & Masson (1995) can be used to explain the momentum distribution along the axis of the redshifted outflow lobe in the hh215 region.

### 4.3. Bow Shocks, Jets, and Wide-Angle Winds

The temperature distribution, the kinematics, the momentum distribution, and the morphology of the outflow gas may all be used to deduce the most likely entrainment mechanism responsible for the molecular outflow. In this section we summarize our results and discuss which are the most likely entrainment mechanisms that accelerate the molecular gas of the outflow associated with PV Cep.

#### 4.3.1. Blueshifted CO Bow Shocks in HH 315C and HH 315B

In Table 5 we list the properties of the outflow gas associated with HH 315B. The morphology as well as the temper-

ature, velocity, and momentum distributions of the outflow gas are all consistent with bow shock entrainment models. Thus, we conclude that the outflow gas associated with HH 315B is bow shock driven.

In Table 6 we list the characteristics of the molecular outflow gas associated with HH 315C. Some of the properties listed are consistent with both bow shock and wide-angle–wind entrainment. As discussed below, HH 315 is an episodic outflow, in which HH 315C and HH 315B come from consecutive episodes. The mass ejection episode responsible for HH 315B entrains the ambient gas with a bow shock, so the same is expected for HH 315C. It is highly unlikely that two consecutive mass ejection episodes interact with the environment through two different mechanisms. Thus, we suspect that the outflow gas associated with HH 315B and that associated with HH 315C are both produced by the bow shock entrainment of an episodic jet.

We note that there is still the possibility that the underlying stellar wind that produces the outflow in this area is technically not a jet bow shock but a very collimated angle-dependent wind. How a wide-angle wind interacts with the ambient gas depends on the angular distribution of the wind force (e.g., Matzner & McKee 1999 and references therein). If the wind force is highly concentrated on the pole, then the wind would essentially be jetlike. This jetlike wind would interact with the ambient medium very much like a bona fide jet. Thus, outflows created by a highly collimated angle-dependent wind and outflows created by a jet show very similar morphologies and velocity and momentum distributions—any differences would be indistinguishable by our observations. Thus, a very collimated angle-dependent wind and a bona fide jet will produce practically the same entrainment mechanism.

TABLE 6

COMPARISON OF MOLECULAR OUTFLOW ASSOCIATED WITH HH 315C AND RESULTS FROM ENTRAINMENT MODELS

| | | | CONSISTENT WITH MODEL? | | |
|---|---|---|---|---|---|
| PARAMETER | DESCRIPTION | FIGURE | Turbulent Jet | Bow Shock | Wide-Angle Wind |
| Morphology........ | Large and wide shell-like (or bowlike), with wings extending in direction of outflow source | 3 | No | Yes | Yes |
| Temperature ....... | $T_{ex}$ of outflow greater than ambient $T_{ex}$, also increase in $T_{ex}$ with velocity | 11 | No | Yes | No |
| Velocity .............. | Double-peaked velocity distribution | 13 | No | No | No |
| Momentum......... | Higher in bow (shell) wings due to underlying ambient density distribution | 14 | No | Yes | Yes |

TABLE 7

COMPARISON OF REDSHIFTED MOLECULAR OUTFLOW LOBE SOUTH OF PV CEPHEI AND RESULTS FROM ENTRAINMENT MODELS

| | | | CONSISTENT WITH MODEL? | | |
|---|---|---|---|---|---|
| PARAMETER | DESCRIPTION | FIGURE | Turbulent Jet | Bow Shock | Wide-Angle Wind |
| Morphology........ | Jetlike, with wiggling axis | 17 | Yes | Yes | No |
| Temperature ....... | Outflow $T_{ex}$ greater than ambient $T_{ex}$, with local maxima at source position and $\sim 60''$ south of source along axis | 12 | No | Yes[a] | No |
| Velocity .............. | Velocity peak at source and $\sim 60''$ south of source | 15 | No | Yes[b] | No |
| Momentum......... | Maximum at source, general decrease with distance from source | 16 | No | Yes[c] | No |

[a] Consistent with bow shock entrainment by several internal working surfaces, each responsible for the rise in temperature.
[b] Consistent with bow shock entrainment by several internal working surfaces, each responsible for the rise in velocity. Note, most of the low-velocity redshifted emission at the source position is *not* due to the PV Cep outflow.
[c] Consistent with bow shock entrainment with an underlying ambient density gradient of $r^{-a}$, where $1 \le a \le 2$.

### 4.3.2. *The Redshifted* CO *Jet South of PV Cep*

The properties of the redshifted molecular outflow lobe (south of PV Cep in the hh215 region) are listed in Table 7. The redshifted outflow gas in this region shows a clear jetlike (very collimated) structure that extends south of PV Cep (see Fig. 17). Turbulent entrainment has been proposed as an attractive model to explain other molecular outflows with similar highly collimated morphologies (e.g., HH 211, Gueth & Guilloteau; NGC 2024, Richer et al. 1992). But, as can be seen in Table 7, the morphology is the only characteristic of the redshifted outflow lobe that is consistent with turbulent jet entrainment models.

Bow shock entrainment by a variable jet with internal working surfaces seems to better explain our results. A major internal working surface at $\sim 60''$ (0.15 pc) south of PV Cep may naturally explain all of the following characteristics that are seen there: (1) the local increase in outflow gas column density (i.e., outflow clump or hot spot) seen in Figure 6d; (2) the slight rise in the CO line ratio (Fig. 12); and (3) the peak in outflow velocity (Fig. 15). We thus conclude that the redshifted outflow gas south of PV Cep has most likely been entrained by a variable jet with internal bow shocks.

The chain of optical HH knots that form HH 215 is also highly suggestive of a variable jet morphology. The average axis of HH 215 is coincident with the general north-south axis of the redshifted molecular outflow lobe south of PV Cep (see Fig. 17). The HH 215 knots show a wiggling pattern somewhat similar to the redshifted outflow lobe axis (see Fig. 17). In addition, HH 215(1)—the brightest knot in HH 215—is $\sim 55''$ north of PV Cep. Thus, we strongly believe that the redshifted molecular outflow is entrained by the counterjet of HH 215 and that the features observed $\sim 60''$ south of PV Cep are produced by the counterknot of HH 215(1).

It is interesting to note that although the outflow gas in the hh315b+c region (Fig. 3) and the redshifted outflow in the hh215 region, south of PV Cep (Fig. 17), are both presumably entrained by the same mechanism, they have very different morphologies. The source of this seeming inconsistency is apparent from the morphology of the optical HH 315 flow. Similar to other HH flows (e.g., HH 34 [Reipurth et al. 1986; Devine et al. 1997] and HH 111 [Reipurth, Raga, & Heathcote 1992; Reipurth et al. 1997b; RBD]), the HH objects that make up HH 315 increase in size the further away they are from the outflow source. We should expect

the redshifted counterknots of HH 215, south of PV Cep, to be as compact and small as HH 215. Therefore, the redshifted gas south of PV Cep has a jetlike appearance because it is most probably entrained by a continuous (unresolved) chain of small bow shocks that have a jetlike appearance.
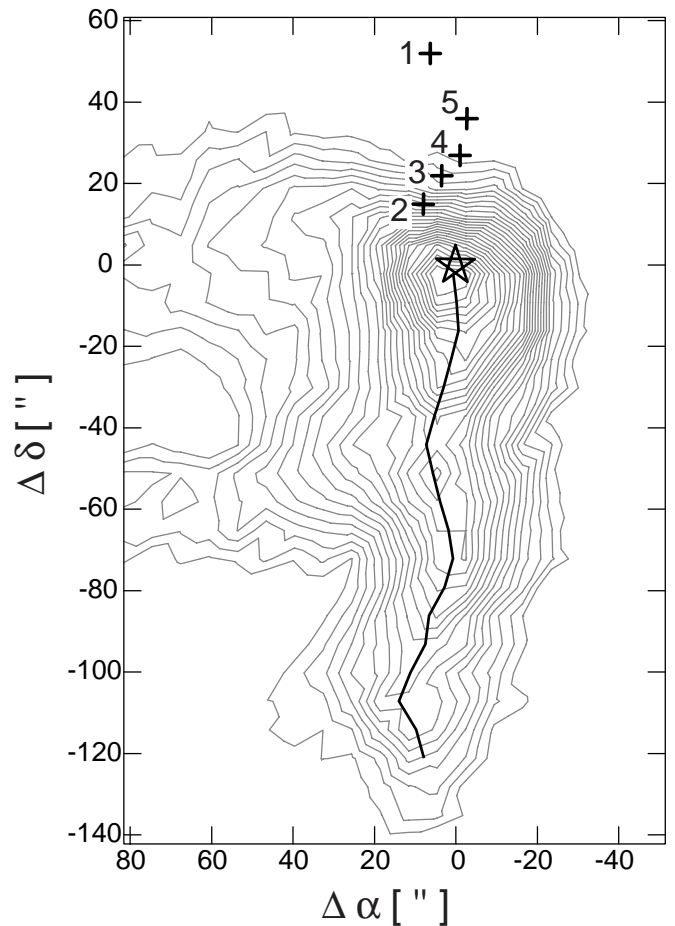


FIG. 17.—$^{12}$CO (2–1) integrated intensity contours of the wiggling molecular redshifted outflow lobe in the hh215 region, near PV Cep. The contours are the same as the left panel of Fig. 12. The emission centroid (obtained from Gaussian fits to the intensity profile) is indicated by the thick black line. The star symbol represents the position of PV Cep. The plus signs represent the position of the HH 215(1) through HH 215(5) knots, and the number beside each plus sign indicates the HH 215 knot number.

On the other hand, the transverse size of the bow shock responsible for the blueshifted outflow associated with HH 315C is larger than the shocks associated with HH 215, and so the CO outflow bow shock–like structure produced is very well resolved by our observations.

#### 4.3.3. *Evidence for a Blueshifted Wide-Angle Wind North of PV Cep*

The blueshifted $^{12}CO$ and $^{13}CO$ gas just north of PV Cep, in the hh215 region, shows a wide-angle structure. The $^{13}CO$ integrated emission has a V-like structure that encloses the blueshifted emission seen in $^{12}CO$ (see Fig. 8). In addition, the $^{13}CO$ V-structure coincides with the walls of the optical conical reflection nebula. Thus, we are confident that the observed blueshifted $^{13}CO$ structure traces the limb-brightened walls of a wind-blown cavity. This structure is similar to that observed in the inner regions of the B5–IRS 1 outflow (Langer, Velusamy, & Xie 1996; Velusamy & Langer 1998; YBB).

Approximately coincident with the cavity axis lies the HH 215 chain of knots. These optical knots trace gas that has recently been excited by a very collimated wind—which seems to be very different from the wide-angle wind responsible for the V-shaped cavity. One explanation that could explain the observations is that there are two different wind components in the northern (blueshifted) lobe close to PV Cep: (1) a collimated (jetlike) wind responsible for the HH 215 knots and (2) a wide-angle wind responsible for the poorly collimated blueshifted $^{12}CO$ immediately north of PV Cep and the $^{13}CO$ V-shaped structure. A similar two-component wind is observed in the inner region of the B5–IRS 1 outflow (see YBB).

There is evidence that a " dual-wind component " is also present in the southern (redshifted) lobe of the outflow associated with PV Cep. As discussed above, the collimated outflow lobe south of PV Cep is most probably produced by a variable jet (the counter jet of HH 215). We do not detect a wide-angle wind in the redshifted lobe south of PV Cep, but optical observations of the region close to PV Cep (Gledhill et al. 1987; Levreault & Opal 1987; Neckel et al. 1987; RBD) have detected a fan-shaped reflection nebula south of PV Cep, similar to the reflection nebula north of PV Cep (see Fig. 8). It is very probable that the redshifted molecular gas emission of the wide-angle wind south of PV Cep is "hidden " under the optically thick ambient cloud emission of the region.

If the above picture is correct, a model that allows for the coexistence of both a wide-angle and a very collimated wind is needed to explain the outflow from PV Cep, similar to the B5–IRS 1 outflow (YBB). So, we believe, as YBB do for B5–IRS 1, that the sum of all the observations of the PV Cep outflow near the source can be best described with a two-component–wind model (like that of Hirose et al. 1997) or a single-wind model in which the wind splits into a very collimated (axial) component and a wide-angle component (like the X-wind model of Shu et al. 1995 and references therein; see also Shang, Shu, & Glassgold 1998).

Alternatively, as proposed to us by the anonymous referee, the wide-angle cavity could be a result of the episodic and precessing nature of the HH 315 flow. Sideways splashing from each HH flow episode could, in principle, slowly burrow through the ambient gas, creating a wide-angle cavity without the need of invoking another (wide angle) wind

component. Although it is possible that a wide-angle cavity could be formed in such a way, we find that this picture does not entirely fit the observations of PV Cep. For example, sideways splashing from the HH 315C, B, and A episodes would have helped formed a cavity with an axis tilted toward the west, unlike the observed nice V-shaped cavity with an almost perfect north-south axis. Also, the V-shaped cavity is unlikely to have been produced solely by the sideways splashing of the HH 215 episode since the cavity extends more toward the north than the HH 215 chain of optical knots. Thus, we prefer a wide-angle–wind component in order to explain the existing observational data. Further kinematic studies of the molecular gas near PV Cep should help clarify the nature of the wide-angle cavity.

### 4.4. *Episodicity and Axis Wandering of the HH 315 Flow*

#### 4.4.1. *Episodicity*

Previous optical studies have pointed out the possible episodic nature of the HH 315 giant HH flow (GKW, RBD). The optical evidence for the episodicity of HH 315 comes from the fact that each of the three major HH knots in each lobe is about 0.35 pc from each other, with no HH-like emission between them. An HH knot is produced by the shock arising from the interaction of a high-velocity flow of gas ejected by a young star and the ambient medium. In HH 315, the HH knot pairs C-F, B-E, and A-D (see Fig. 2) are thought to arise from three different mass ejection episodes.

Our millimeter-line data show further evidence for the episodic nature of the HH 315 flow. The outflow gas surrounding the HH 315B and HH 315C knots has a spatially discrete structure (Fig. 3) that shows a shell-like or bowlike structure at the position of each of the two knots. At the head of each of these shell-like structures there is an increase in outflow velocity (Fig. 13). A velocity increase at the position of the optical HH knots A, B, C, and D is also observed in the large-scale $^{12}CO$ (2–1) *p-v* diagram of the HH 315 outflow (Fig. 13 in Paper I). Such morphology and velocity distribution in the molecular outflow gas is not expected if the underlying stellar wind responsible for the creation of the molecular outflow were made of a continuous constant flow of ejected mass. The multiple CO shell structure and the peak molecular outflow velocity at the head of the shock (the position of the HH knot) are better understood if the molecular outflow from PV Cep is formed by a wind with sporadic episodes of copious mass loss (see also Arce & Goodman 2001a).

#### 4.4.2. *Wandering Ejection Axis*

The fact that the ejection axis of HH 315 changes over time has been well established by the optical images of the flow, where it is clearly seen that the HH knots trace an S-shaped path. Tracing a line from PV Cep to the location of each knot, it is seen that each major knot has a different position angle on the sky. Each mass ejection should travel in a straight line after being ejected by the young star, unless it collides with a dense clump that could change its trajectory. Our large-scale molecular gas maps (Paper I) do not show any evidence for dense clumps that could have perturbed the ballistic trajectory of any ejection. Thus, the HH knots in HH 315 are at different angles with respect to PV Cep, because PV Cep's angle of ejection is changing over time (i.e., wandering or precessing). GKW have successfully reproduced the morphology of the HH 315 flow with a sim-

ple precession model, assuming a jet velocity of 200 km s$^{-1}$, a precession cone with full opening angle of $\sim 45°$, an inclination to the plane of the sky of $\sim 10°$, and a precession period of about 8300 yr. A. A. Goodman & H. G. Arce (2002, in preparation) show that a westward motion of PV Cep, in addition to a time-varying ejection angle, explains the position of the HH knot pairs (A-D, B-E, and C-F) with respect to the source better than models without transverse source motion.

In addition to the "precession" (or change in ejection angle) traced by the optical HH knots, our millimeter CO data for the redshifted outflow gas in the hh215 region show signs of a small-scale time-varying ejection angle. In Figure 17 we show the integrated intensity contours of the red-shifted gas in the hh215 region, integrated over the velocity range where we detect outflow emission. We made east-west intensity cuts for all pixel rows, for the extent of the north-south (jetlike) outflow structure. Most of the cuts show Gaussian-like intensity profiles, so we fitted a Gaussian to each cut and obtained the position of the Gaussian centroid from each fit. In Figure 17, the thick black solid line plotted over the intensity contours indicates the position of the integrated emission centroid (obtained from the Gaussian fit) along the length of the redshifted CO jetlike structure. Assuming that the emission centroid indicates the position of the outflow axis, we can state that the axis varies in direction over time (it wiggles). Similar wiggling morphology has been detected in optical HH jets (e.g., Heathcote et al. 1996) and other molecular outflows (Davis et al. 1997).

In Figure 18a we plot the presumed trajectory of the jet axis, traced by the $^{12}$CO (2–1) velocity-integrated intensity centroid. It can be seen in Figure 18a that the points trace a sine-like path with a slope. We fit the centroid path with a straight line, and we then subtract the fit to the points and show the result in Figure 18b. A sine wave was subsequently fitted to the slope-corrected points (see Fig. 18b). Notice that the points at the peaks and valleys (of the sinusoidal trace) increasingly deviate from the sine fit, the farthest away from the source. This behavior, where the axis traces a cone (projected on the plane of the sky) rather than a cylinder, is suggestive of a "precession cone" expected for a flow with a quasi-periodic time-varying ejection axis (due to pure periodic precession or to a quasi-periodic random wandering of the ejection axis).

Assuming that the sinusoidal appearance of the red-shifted lobe comes from a purely periodic precession in the ejection axis, we may use the "wavelength" ($\lambda \sim 28,820$ AU) of the sine fit made to the points in Figure 18b to obtain a precession period. If we assume a jet velocity of 200 km s$^{-1}$ (the same as GKW and RBD), we then obtain a precession period ($T = \lambda / v_{jet}$) of $\sim 680$ yr.

Tidal interactions between binary components and a circumstellar disk is one possible mechanism that could induce precession on a young star. Terquem et al. (1999) give an approximate expression for the precession period of a disk around a young star in a binary system, where the disk surrounds only the primary star. The expression is given in terms of the primary mass ($M_p$), the mass ratio of the two stars, the disk radius ($R$), and the binary separation ($D$). Observations show that if PV Cep has a binary companion it must be less than 50 AU apart (Leinert, Richichi, & Hass 1997). We can use equation (1) in Terquem et al. (1999) and solve for the binary separation, to see if a precession period of $\sim 680$ yr is possible for a binary system with a separation
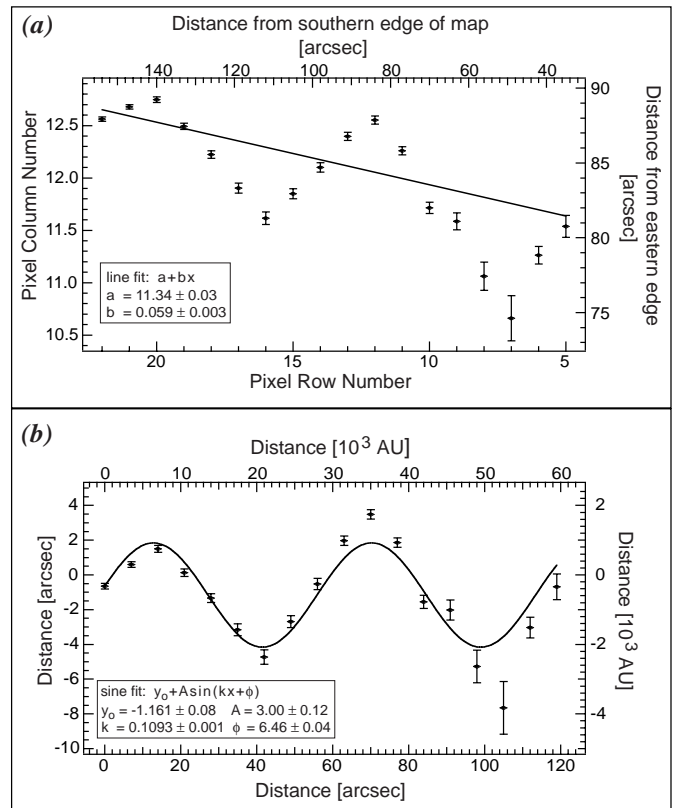


FIG. 18.—(a) Plot of the redshifted outflow lobe emission centroid position. Distances are given in terms of pixel numbers and arcseconds from the map (Fig. 17) edges. The straight-line fit to the points is plotted, and the fit parameters are shown. (b) Plot of the redshifted outflow lobe emission centroid position, corrected for the slope indicated by the line fit in (a). The sinusoidal fit to the points and the resultant fit parameters are shown. Axes are in arcsecond offsets and distance in AU from the source. In both panels, the errors shown are 3 $\sigma$ errors.

of less than 50 AU between its members. If we assume PV Cep is the primary star with a mass of 4 $M_{\odot}$ (Fuente et al. 1998), a primary-to-secondary mass ratio of about 0.25, and a 15 AU disk radius, then a binary separation of $\sim 21$ AU would be needed to drive a precession with a period of 680 yr. Even if we were to change our assumptions to a primary-to-secondary mass ration of 1 and a disk radius of 25 AU, the binary separation would be 43 AU. Thus, it is possible that the wiggling of the jet is due to precession of the outflow source induced by tidal interactions between PV Cep, a yet undetected binary companion, and PV Cep's circumstellar disk.

The precession period of $\sim 680$ yr, from our observations of the wiggling redshifted CO outflow lobe, is about a factor of 12 less than the precession period obtained by GKW (from modeling the trajectory traced by the optical HH knots in HH 315). This apparent difference in precession period seems to indicate that (1) the precession period is changing over time or (2) there are two different mechanisms that are responsible for the different apparent precession-like motions.

Theoretically, the ejection of a third companion in a hierarchical triple system could lead to the formation of a tighter binary (see Reipurth 2000 for more details). But, in the case of PV Cep the tightening of the binary system

would have to occur in a very short timescale of 2000 yr.[3] In addition, it is extremely coincidental that we would be observing PV Cep right at the moment after the tightening of the binary system. Thus, it is unlikely that this scenario applies to PV Cep. It seems more likely, then, that the large-scale axis wandering is due to some other (unknown) mechanism. Some other possible mechanisms that could produce precession-like motions of the outflow ejection axis are changes in the outflow source's magnetic field orientation or a precession-like motion induced by tidal interactions of *multiple* stellar companions and their circumstellar disks.

In summary, we may explain the short-timescale axis wandering observed in the HH 315 outflow by circumstellar disk precession. However, it is highly unlikely that the same mechanism is responsible for the large-scale axis wandering.

## 5. SUMMARY

We observed, at high velocity and spatial resolution, the molecular gas surrounding several knots of the giant Herbig-Haro flow HH 315 from the young star PV Cep. The observations were aimed at studying the interaction between the HH flow and the ambient gas. The data obtained include simultaneous observations, at the IRAM 30 m telescope, of the $^{12}$CO (1–0), $^{12}$CO (2–1), and $^{13}$CO (1–0) molecular lines. The three regions observed include (1) an area surrounding two blueshifted knots (HH 315C and HH 315B) about 0.9–1.2 pc northwest of PV Cep; (2) an area that includes the gas surrounding the outflow source, the HH 215 blueshifted optical knots ~0.05–0.15 pc north of PV Cep, and the collimated redshifted molecular gas south of PV Cep; and (3) an area surrounding the redshifted optical knot HH 315E, about 0.9 pc southeast from the outflow source. The main points derived from our study can be summarized as follows:

1. We find that the blueshifted outflow gas in the region surrounding HH 315B and HH 315C has clearly been accelerated by bow shock entrainment of an episodic jet. The molecular outflow gas shows a spectacular bow shock–shaped morphology, which has a width of about 0.4 pc at the slowest outflow velocities. The head of the CO outflow bow structure coincides with the position of the bow-shaped optical knot HH 315C. There is also blueshifted molecular outflow gas coincident with the optical knot HH 315B that exhibits a structure suggestive of a bow shock morphology. A bowlike structure coincident with each knot and the fact that both the excitation temperature and the velocity of the outflow gas show peaks at the position of the head of each bowlike structure are both consistent with an outflow formed by two different bow shocks. Each of these two bow shocks was formed by a different mass ejection episode, where HH 315C is the "leading jet head" of the HH 315 giant flow and HH 315B is a shock formed by a subsequent mass ejection episode.

2. Near PV Cep (within 0.3 pc), the observational data is highly suggestive of the coexistence of a wide-angle wind and a collimated (jetlike) wind. The blueshifted $^{13}$CO integrated emission shows a V-shaped morphology with an opening angle of ~90°, which is coincident with an optical reflection nebula. The blueshifted $^{12}$CO has a fanlike morphology that fills the cavity delineated by the $^{13}$CO V-shaped structure. We suggest that the $^{13}$CO traces the limb-brightened walls of a wide-angle wind blown cavity. Along the axis of the wide-angle blueshifted $^{12}$CO outflow lie the previously detected optical knots HH 215. These small knots delineate the collimated component of the blueshifted wind north of PV Cep.

3. We find that the redshifted molecular outflow lobe south of PV Cep is most likely entrained by a variable jet with several internal working surfaces (bow shocks). The redshifted outflow has a collimated wiggling jet–like appearance, with an "average" north-south axis, which extends to about 0.3 pc south of PV Cep. The momentum distribution is consistent with jet bow shock entrainment in an ambient medium with density decreasing with distance from the source. Also, the velocity and temperature distribution of the molecular outflow gas are consistent with its being entrained by a jet with several internal bow shocks. We show that the same (bipolar) mass ejection episode responsible for the blueshifted HH 215 optical knots (north of PV Cep) is also responsible for the entrainment of the redshifted outflow lobe. There has been no optical detection of the redshifted counterjet of HH 215 because of the heavy extinction in the region south of PV Cep.

4. We find that the wiggling observed in the redshifted CO outflow lobe near PV Cep is most probably due to a time-varying ejection axis. Assuming that the wiggling is due to precession of the outflow source, and a jet velocity of 200 km s$^{-1}$, then the precession period is 680 yr. This is about a factor of 10 less than the precession period deduced from the large-scale optical HH flow. We may explain the short-timescale axis wandering observed in the redshifted molecular outflow lobe by precession induced by tidal interactions between (undetected) binary companions and a circumstellar disk. However, it is highly unlikely that the same mechanism is responsible for the large-scale axis wandering.

5. We do not detect any outflow emission in the region surrounding the HH 315E optical knot. The CO spectra in this region has an FWHM width of only ~1 km s$^{-1}$ and shows no evidence of outflow–ambient gas interaction. It is puzzling to find such a narrow CO width in a region presumably affected by a stellar outflow. It is probable that all of the CO observed in the direction of HH 315E is in front of HH 315E (on the same line of sight) and that HH 315E is interacting mainly with atomic gas behind the molecular cloud.

[3] This is the approximate timescale between the eruptions responsible for the HH 215 chain of knots and the HH 315A-D knot pair (see Fig. 2), assuming $v_{jet} \sim 200$ km s$^{-1}$.

## REFERENCES

Arce, H. G., & Goodman, A. A. 2001a, ApJ, 551, L171
———. 2001b, ApJ, 554, 132
———. 2002, ApJ, 575, 911 (Paper I)
Bachiller, R., & Tafalla, M. 1999, in The Origin of Stars and Planetary Systems, ed. C. J. Lada & N. D. Kylafis (NATO ASI Ser. C, 540; Dordrecht: Kluwer), 227
Bence, S. J., Richer, J. S., & Padman, R. 1996, MNRAS, 279, 866
Cabrit, S., & Raga, A. 2000, A&A, 354, 667
Cantó, J., & Raga, A. C. 1991, ApJ, 372, 646
Cantó, J., Raga, A. C., & D'Alessio, P. 2000, MNRAS, 313, 656
Cernicharo, J., & Reipurth, B. 1996, ApJ, 460, L57
Chernin, L. M., & Masson, C. R. 1995, ApJ, 455, 182
Cliffe, J. A., Frank, A., & Jones, T. W. 1996, MNRAS, 282, 1114
Cohen, M., Kuhi, L. V., Harlan, E. A., & Spinrad, H. 1981, ApJ, 245, 920
Davis, C. J., Dent, W. R. F., Matthews, H. E., Coulson, I. M., & McCaughrean, M. J. 2000, MNRAS, 318, 952
Davis, C. J., Eislöffel, J., Ray, T. P., & Jenness, T. 1997, A&A, 324, 1013
Davis, C. J., Smith, M. D., & Moriarty-Schieven, G. H. 1998, MNRAS, 299, 825
Devine, D., Bally, J., Reipurth, B., & Heathcote, S. 1997, AJ, 114, 2095
Downes, T. P., & Ray, T. P. 1999, A&A, 345, 977
Fuente, A., Martín-Pintado, J., Bachiller, R., Neri, R., & Palla, F. 1998, A&A, 334, 253
Gledhill, T. M., Warren-Smith, R. F., & Scarrott, S. M. 1987, MNRAS, 229, 643
Gómez, M., Kenyon, S., & Whitney, B. A. 1997, AJ, 114, 265 (GKW)
Gueth, F., & Guilloteau, S. 1999, A&A, 343, 571
Hartigan, P., Bally, J., Reipurth, B., & Morse, J. A. 2000, in Protostars and Planets IV, ed. V. Mannings, A. P. Boss, & S. S. Russell (Tucson: Univ. Arizona Press), 867
Hatchell, J., Fuller, G. A., & Ladd, E. F. 1999, A&A, 344, 687
Heathcote, S., Morse, J. A., Hartigan, P., Reipurth, B., Schwartz, R. D., Bally, J., & Stone, J. M. 1996, AJ, 112, 1141
Hirose, S., Uchida, Y., Shibata, K., & Matsumoto, R. 1997, PASJ, 49, 193
Lada, C. J., & Fich, M. 1996, ApJ, 459, 638
Langer, W. D., Velusamy, T., & Xie, T. 1996, ApJ, 468, L41
Lee, C.-F., Mundy, L. M., Reipurth, B., Ostriker, E. C., & Stone, J. M. 2000, ApJ, 542, 925
Lee, C.-F., Stone, J. M., Ostriker, E. C., & Mundy, L. G. 2001, ApJ, 557, 429
Leinert, C., Richichi, A., & Hass, M. 1997, A&A, 318, 472
Levreault, R. M. 1984, ApJ, 277, 634

Levreault, R. M., & Opal, C. B. 1987, AJ, 93, 669
Li, Z.-Y., & Shu, F. H. 1996, ApJ, 472, 211
Lizano, S., & Giovanardi, C. 1995, ApJ, 447, 742
Masson, C. R., & Chernin, L. M. 1993, ApJ, 414, 230
Matzner, C. D., & McKee, C. F. 1999, ApJ, 526, L109
Neckel, T., Staude, H. J., Sarcander, M., & Birkle, K. 1987, A&A, 175, 231
Raga, A., & Cabrit, S. 1993, A&A, 278, 267
Raga, A. C., Cantó, J., Binette, L., & Calvet, N. 1990, ApJ, 364, 601
Raga, A. C., & Kofman, L. 1992, ApJ, 386, 222
Reipurth, B. 2000, AJ, 120, 3177
Reipurth, B., & Bally, J. 2001, ARA&A, 39, 403
Reipurth, B., Bally, J., & Devine, D. 1997a, AJ, 114, 2708 (RBD)
Reipurth, B., Bally, J., Graham, J. A., Lane, A. P., & Zealey, W. J. 1986, A&A, 164, 51
Reipurth, B., Hartigan, P., Heathcote, S., Morse, J. A., & Bally, J. 1997b, AJ, 114, 757
Reipurth, B., Raga, A. C., & Heathcote, S. 1992, ApJ, 392, 145
Richer, J. S., Hills, R. E., & Padman, R. 1992, MNRAS, 254, 525
Rohlfs, K., & Wilson, T. L. 2000, Tools of Radio Astronomy (3d ed.; New York: Springer)
Scarrot, S. M., Rolph, C. D., & Tadhunter, C. N. 1991, MNRAS, 249, 131
Shang, H., Shu, F. H., & Glassgold, A. E. 1998, ApJ, 493, L91
Shepherd, D. S., Yu, K. C., Bally, J., & Testi, L. 2000, ApJ, 535, 833
Shu, F. H., Najita, J., Ostriker, E. C., & Shang, H. 1995, ApJ, 455, L155
Shu, F. H., Ruden, S. P., Lada, C. J., & Lizano, S. 1991, ApJ, 370, L31
Smith, M. D., Suttner, G., & Yorke, H. W. 1997, A&A, 323, 223
Stahler, S. W. 1994, ApJ, 422, 616
Stone, J. M., & Norman, M. L. 1993a, ApJ, 413, 198
———. 1993b, ApJ, 413, 210
———. 1994, ApJ, 420, 237
Suttner, G., Smith, M. D., Yorke, H. W., & Zinnecker, H. 1997, A&A, 318, 595
Taylor, S. D., & Williams, D. A. 1996, MNRAS, 282, 1343
Terquem, C., Eislöffel, J., Papaloizou, J. C. B., & Nelson, R. P. 1999, ApJ, 512, L131
Velusamy, T., & Langer, W. D. 1998, Nature, 392, 685
Wild, W. 1999, The 30m Manual: A Handbook for the IRAM 30m Telescope (St-Martin-d'Hères: IRAM)
Wolfire, M. G., & Königl, A. 1993, ApJ, 415, 204
Wu, Y., Huang, M., & He, J. 1996, A&AS, 115, 283
Yu, K. C., Billawala, Y., & Bally, J. 1999, AJ, 118, 2940 (YBB)
Zhang, Q., & Zheng, X. 1997, ApJ, 474, 719